

11-45-CR
0.07
300'15"

**MEASUREMENT OF HO₂ AND OTHER TRACE GASES IN THE STRATOSPHERE
USING A HIGH RESOLUTION FAR-INFRARED SPECTROMETER**

NASA GRANT NSG 5175

Semiannual Status Report No. 33

For the period 1 July 1993 to 31 December 1993

Principal Investigators

Wesley A. Traub
Kelley V. Chance

January 1994

Prepared for

National Aeronautics and Space Administration

Greenbelt, Maryland 20771

Smithsonian Institution
Astrophysical Observatory
Cambridge, Massachusetts 02138

**The Smithsonian Astrophysical Observatory
is a member of the
Harvard-Smithsonian Center for Astrophysics**

The NASA Technical officer for this grant is Dr. William S. Heaps, Code 916, Atmospheric Experiments Branch, Goddard Space Flight Center, Greenbelt, Maryland 20771

N94-24738

Unclas

0206757

G3/46

(NASA-CR-195173) MEASUREMENT OF
HO₂ AND OTHER TRACE GASES IN THE
STRATOSPHERE USING A HIGH
RESOLUTION FAR-INFRARED
SPECTROMETER Semiannual Status
Report No. 33, 1 Jul. - 31 Dec.
1993 (Smithsonian Astrophysical
Observatory) 36 p

Semiannual Report No. 33

NASA Grant NSG-5175

Measurement of HO₂ and Other Trace Gases in the Stratosphere Using a High Resolution Far-Infrared Spectrometer

1. Personnel Working Under this Grant During this Reporting Period

Dr. Wesley A. Traub (Principal Investigator)

Dr. Kelly V. Chance (Principal Investigator)

Dr. David G. Johnson (Co-Investigator)

Dr. Kenneth W. Jucks (Co-Investigator)

Dr. Steven C. Wofsy (Co-Investigator)

Dr. Changqin (Jim) Xue (Programmer-Analyst)

Ms. Paola Ciarpallini (SAO Predoctoral Fellow)

2. Status Summary

This report covers the time period 1 July 1993 to 31 December 1993. We had no balloon or airplane flights during this reporting period, concentrating instead on analyzing our existing data. Having completed an extensive program of enhancing and validating our data reduction software, we are using our data sets to examine the changes in stratospheric chemistry over a variety of time scales. Ongoing projects include investigating the diurnal variation of OH, HO₂, and H₂O₂ and exploring their relationships with other simultaneously measured species; measuring long term trends in HF and HCl; and looking for changes caused by the June 1991 Pinatubo eruption. We are also continuing to analyze the large set of data collected during the AASE II.

3. AASE II

We completed a paper on stratospheric subsidence during this reporting period. The paper has been submitted to JGR, and is included as an appendix to this report. The analysis begun during the last reporting period has been completed, and we have repeated the water and low latitude subsidence measurements using an improved hydropause model. In the coming months we plan to study the significance of the observed trends in the concentrations of HCl, O₃, H₂O, and HNO₃ as a function of time and potential vorticity.

4. UARS Correlative Measurements Program

We have repeated our analysis of N₂O for the May 1992, September 1992, and March 1993 correlative balloon flights, using an improved set of values for the ν_2 fundamental line strengths obtained from J. W. C. Johns. The new line strengths differ from the values in the HITRAN92 line catalog by amounts in excess of 20%, and so our retrieved mixing ratios have changed substantially. We have provided the CLAES group with our revised numbers for comparison. The results for the N₂O and HNO₃ intercomparisons were presented at the December 1993 AGU meeting in San Francisco. We have also compared our measurements of temperature, O₃, H₂O, and NO₂ with CLAES measurements, and with the exception of NO₂ the measurements are generally consistent within the estimated errors.

5. Analysis of Balloon Flight Data

We have used our improved data reduction routines to analyze data from the March 1993, September 1992, May 1992, June 1990, and September 1989 balloon flights, and the analysis of data from the May 1988 balloon flight is well underway. In addition, we are in the process of modifying our software to allow us to analyze data from the FIRS-1 instrument, which operated from 1979–1983. This will give us a data set covering at least a ten year period which we can use to measure changes in the abundances of HCl and HF. In an ongoing project we are comparing the data from 1989 and 1990 to the 1992 and 1993 data to search for the effects of the 1991 Pinatubo eruption. We have already observed a dramatic increase in the abundance of HNO_3 , as well as an increase in the daytime abundance of HOCl from which we infer an increase in ClO.

As part of our ongoing work to check our analysis procedures whenever possible, we are participating in the European Stratospheric MONitoring Stations/Network for the Detection of Stratospheric Change (ESMOSII/NDSC) algorithm intercomparison exercise. Given a standard set of input data, the 16 groups participating in this exercise will use their own algorithms to derive independent column densities for a number of molecules. Our results have been submitted, and we look forward to seeing how they compare with the results of other groups. As one result of this exercise we have corrected our data reduction procedure for the effect of the finite aperture on the instrumental smearing width. While our spectrometer has aperture stops which minimize this effect, the spectra supplied as part of the intercomparison are severely self-apodized.

In addition to comparisons with the CLAES instrument, we have compared our measurements with the simultaneous in-situ ozone measurements of Jim Margitan, and the remote sensing measurements of O_3 , HCl, HNO_3 , and HO_2 made by the SLS instrument, kindly provided by Bob Stachnik. As is the case for our comparisons with CLAES, the measurements agree to within the estimated errors.

For the October 1993 methyl bromide workshop, we analyzed our data from 5 balloon flights in 2 spectral regions (99.9 and 116 cm^{-1}) for evidence of HBr. We derived a weighted mean value of 1.1 ± 1.2 pptv, which we interpret as a $1\text{-}\sigma$ upper limit of 2.3 pptv for HBr, in the 22–40 km region. This investigation is continuing.

6. Chemical Modeling

We have begun to apply our measurements of stratospheric composition to problems in stratospheric chemistry. As a first step in this direction, we are comparing our abundance measurements for the September 1989 balloon flight with 1-D model results provided by Ross Salawitch. We are particularly interested in exploring the diurnal behavior of OH, HO_2 , and H_2O_2 .

We are also investigating the effects of heterogeneous processes on the stratosphere. The eruption of Pinatubo in 1991 increased the aerosol surface area in the middle latitudes by a factor of roughly 100, which should have increased the rates of heterogeneous reactions proportionately. As already mentioned, our extensive data set, covering periods before and after the eruption, enables us to search for subtle changes in the chemistry.

As part of our investigation of stratospheric chemistry, we have developed a method of deriving daytime ClO mixing ratios from our measurements of HOCl, HO_2 , OH, ozone, and temperature. HOCl is in rapid photochemical equilibrium with ClO via the reactions



with rates k_1 , k_2 , and j_3 respectively. By balancing the creation and destruction rates of HOCl, we derive the relation

$$[\text{ClO}] = [\text{HOCl}] \frac{j_3 + k_2[\text{OH}]}{k_1[\text{HO}_2]} \quad (4)$$

The reaction rate constants are estimated using the data in publication JPL 92-20 and our temperature profile. We use LOWTRAN7 to calculate the UV flux, using our measured temperature and ozone profiles and including the contributions from multiple scattering. The photolysis rate is estimated using the calculated flux and the cross sections in JPL 92-20. Finally, we use our measurements of HOCl, OH, and HO₂ to calculate the ClO abundance using Eq. 4. Initial comparisons with ClO profiles obtained simultaneously by Bob Stachnik look very promising.

7. Publications and Presentations

W. A. Traub, K. W. Jucks, D. G. Johnson, and K. V. Chance, Subsidence of the Arctic Stratosphere Determined from Thermal Emission of HF, submitted to JGR.

D. G. Johnson, K. W. Jucks, W. A. Traub, and K. V. Chance, The Smithsonian Stratospheric Far-Infrared Spectrometer and Data Reduction System, submitted to JGR.

K. V. Chance, W. A. Traub, K. W. Jucks, and D. G. Johnson, The Smithsonian Astrophysical Observatory database SAO92, submitted to J. Quant. Spectrosc. Radiat. Transfer.

W. A. Traub, K. W. Jucks, D. G. Johnson, and K. V. Chance, Subsidence of the Arctic Stratosphere Determined from Thermal Emission of HF, paper A51D-1, Fall meeting of the American Geophysical Union, December 6–10, 1993.

K. V. Chance, W. A. Traub, K. W. Jucks, and D. G. Johnson, The 1992 Smithsonian Astrophysical Observatory Line Parameter Database and its Application to Far Infrared Measurements of the Earth's Stratosphere, paper FP4, Atmospheric Spectroscopy Applications, September 8–10, 1993, Reims, France.

K. W. Jucks, W. A. Traub, D. G. Johnson, and K. V. Chance, Atmospheric Observations with Thermal Emission Spectroscopy, paper AO6, Atmospheric Spectroscopy Applications, September 8–10, 1993, Reims, France.

W. A. Traub and D. G. Johnson, Recent Results on HBr in the Stratosphere, Methyl Bromide Workshop, October 28, 1993, Washington, DC.

APPENDIX A

Subsidence of the Arctic Stratosphere Determined from Thermal Emission of HF

Subsidence of the Arctic Stratosphere

Determined from Thermal Emission of HF

Wesley A. Traub, Kenneth W. Jucks, David G. Johnson, and Kelly V. Chance
Harvard-Smithsonian Center for Astrophysics, Cambridge, Massachusetts

Abstract

We determine subsidence in the Arctic stratospheric vortex from measurements of a rotational line of hydrogen fluoride in thermal emission. The data were obtained with the FIRS-2 spectrometer on board NASA's DC-8 aircraft during the AASE-2 campaign, from January through March 1992. A wide range of meteorological conditions was sampled, both inside and outside the polar vortex region. The measured values of subsidence are analysed as a function of both the time of year, and the dynamically conserved quantity, potential vorticity. From this analysis, we draw the following conclusions. (1) Subsidence is strongly correlated with potential vorticity. However, there appear to be other factors, including meteorological conditions, which play a lesser role. (2) The gradient of subsidence with respect to potential vorticity is large and approximately constant across vortex wall, and is small elsewhere. The gradient of subsidence with respect to horizontal distance is dramatically large across the vortex wall. (3) There appears to be substantial descent in the early winter vortex, from the evidence of the observed subsidence in January, and the assumption of zero subsidence at the fall equinox. (4) Descent continues to occur in late winter, with measured vertical velocities similar to that inferred for early winter. The average early and late winter vertical velocity at a representative altitude of 18 km is $0.052(\pm 0.013)$ cm/s. (5) At the measured rate of

subsidence, the time required to flush the stratosphere by one scale height is about 6 months. (6) The region of maximum descent appears to start near the center of the vortex in early winter, and progressively move out to the mid-wall and outer-wall regions in late winter.

1. Introduction

The polar vortex in the winter stratosphere is driven by reduced solar heat input to the absorbing ozone layer, allowing the stratosphere to cool and its pressure to drop. In this picture, a polar low-pressure system develops, outside air starts to move poleward, and the Coriolis force deflects the air to rotate in the same sense as the earth, i.e., cyclonically [e.g., *Schoeberl et al.*, 1992]. As the cooling air sinks and compresses, it is replaced by high-altitude air moving in from lower latitudes. This vertical compression of air, with replacement at the top, produces a downward transformation of mixing-ratio profiles [Toon *et al.*, 1992]. In this paper, we use our measurements of thermal emission from stratospheric hydrogen fluoride (HF), coupled with a subsidence model, to determine vertical displacement in the Arctic vortex during the Northern Hemisphere winter of 1991-92.

2. Observations

The measurements reported here were made during the Arctic Airborne Stratospheric Expedition (AASE 2) in 1992, using our far-infrared spectrometer (FIRS-2) on board the NASA DC-8 aircraft. The FIRS-2 instrument is the same one we have flown on balloon platforms since 1987 [e.g., *Traub*, 1991, 1992], with several adaptations, as follows. The spectrometer views the stratosphere through a side port in the aircraft, sequentially recording thermal emission spectra at elevation angles of 32, 16, 8, 4, 2, 1, and 0°, followed by calibration scans of a hot and a cold blackbody source. This 700-sec cycle is repeated while the aircraft is at or near cruise altitude, except for brief periods when the sun is close to the line of sight. The viewing angles are selected by a tilting mirror, driven by a stepper motor, and controlled by a shaft encoder referenced to the aircraft roll angle as determined by the on-board inertial navigation system. The infrared radiation is focussed by a fixed telescope

mirror, then fed to the spectrometer. These two feed mirrors are rigidly mounted to the spectrometer, and the entire assembly is floated with respect to the aircraft on pneumatic isolators, to reduce vibration and potential interference fringe contrast losses. The aircraft optical window is removed; due to the difficulty of providing a suitable infrared-transmitting window, a pressure-tight enclosure is placed around the input optics, up to the spectrometer's vacuum tank, where a small-diameter polyethylene window admits light into the spectrometer.

The data reported here were obtained on 13 flights of the DC-8, each lasting about 10 hours, distributed as follows: 165 observations from flights on UT dates January 14, 16, 19, 22, and 24, 1992, centered at about UT day Jan. 19.5; 112 observations from February 17, 20, and 22, centered on Feb. 20.4; and 177 observations from March 10, 12, 14, 18, and 20, centered on Mar. 15.3. About 10 percent of the original data were discarded because observing conditions were poor, i.e., the DC-8 was flying through signal-degrading clouds, or it was changing altitude rapidly. The range of latitudes each month is nominally 38°N (Moffett Field, California) to 90°N, except for one flight in February to 15°N (Puerto Rico).

The aircraft pressure altitude is usually about 11 km, with occasional periods at about 10 and 12 km; this means that at poleward latitudes the aircraft is generally above the tropopause.

Since the DC-8 flights covered a substantial fraction of the winter season, and sampled a wide range of latitudes and vortex conditions, and since the FIRS-2 was operating most of the time that the aircraft was at cruise altitude, we anticipate that the observations discussed in this paper can be taken as being broadly representative of conditions in the entire Arctic polar vortex.

The FIRS-2 measures the thermal emission spectrum of the stratosphere against

the cold background of space. Since the radiated power in an emission line is dependent upon the temperature, through the level population and Planck function, and since the temperature in the stratosphere is essentially independent of solar elevation in the short term, we find that long-lived species, such as HF, have spectra which are constant from day to night.

Following *Toon et al.* [1992] and *Mankin et al.* [1990], we use HF as a tracer of vertical motion in the stratosphere. There are three reasons for using this tracer. (a) HF is produced in the stratosphere, starting with photodissociation of chlorofluorocarbons and SF₆, and so has a positive vertical gradient in volume mixing ratio (*vmr*). If an air column is displaced downward, with replacement at the top by air from neighboring columns, then the total column abundance of HF will increase. If the nominal *vmr* profile is known, then the amount of vertical motion can be quantified from measurements of the change in column abundance. (b) HF is expected to be chemically unreactive, so abundance changes can be attributed to dynamical rather than chemical activity [*Brasseur and Solomon*, 1984]. (c) HF has an easily-measured emission line in the FIRS-2 far-infrared spectrum.

3. Data Analysis

Our data reduction procedures for both balloon and aircraft spectra are presented in detail elsewhere [*Johnson et al.*, 1993], so the present discussion is limited to the most pertinent steps. For HF, we analyze spectra from the upper four elevation angles only, since spectra from the lower three angles have reduced sensitivity due to water vapor opacity in the HF region. The HF line is a rotational transition which lies at 163.936 cm⁻¹. In the high-frequency wing of this line there is a weak hot-band line of water vapor; from an examination of our balloon spectra, which show this region at high signal-to-noise ratio and with reduced pressure broadening,

the catalogued position of this line is found to be incorrect, so it is changed in our line list from 163.9602 to 163.9650 cm^{-1} .

For each spectrum obtained along the flight path, the overhead atmosphere is modeled with a 9-layer model; input parameters include atmospheric pressure at aircraft altitude, and the atmospheric temperature profile. All meteorological data were provided by the Goddard theory group [e.g., *Schoeberl et al.*, 1992], from National Meteorological Center (NMC) data, in the form of a curtain file, *i.e.*, as a function of latitude and longitude along the flight track.

The model *vmr* profile is taken to have a fixed amplitude, but variable vertical scale. The atmosphere is assumed to contract by the factor $(1 + s)$, where s is independent of altitude, but may vary with time; s is the dimensionless “degree of subsidence” (hereafter “subsidence”) parameter introduced by *Toon et al.* [1992]. In other words, we assume that, for a given parcel of air, the quantity $(1 + s)z$ is conserved with respect to changes in latitude, longitude, and time. With this scale transformation, the *vmr* becomes

$$vmr(z) = vmr_0[(1 + s)z_0].$$

Here $vmr_0(z_0)$ is a reference profile appropriate to mid-latitude conditions, with time-trending species (e.g., HF) scaled to expected 1992 values. (The reference profile was kindly supplied by G. Toon [*private communication*, 1993]),

For each spectrum, we iteratively vary the subsidence until the theoretical spectrum matches the observed spectrum in the neighborhood of the HF line, using a least-squares fitting procedure. Both HF and H_2O are scaled with the same value of subsidence; no attempt was made to adjust H_2O independently, since the H_2O line has little effect on the HF feature. The fitting program provides estimates for s and the uncertainty Δs . A weighted mean subsidence and uncertainty in the mean

are calculated from the four independently-determined values in each limb-scan sequence.

As mentioned above, winter-time cooling of the stratosphere causes the air pressure to decrease and the air to become denser, which in turn generates a cyclonic motion in the horizontal plane along with a sinking motion in the vertical direction. In this picture, stratospheric rotation and sinking are both driven by cooling, so in a simple model these effects are functionally related. In the actual atmosphere there are many competing mechanisms which will tend to degrade any straightforward functional relationship. But if rotation and sinking are the dominant effects we should be able to observe a correlation between parameters which measure these motions.

Rotational motion is well-characterized by the potential vorticity (PV) parameter (e.g., [*Brown*, 1991]; [*Peizoto and Oort*, 1992]), which is derived from satellite measurements of temperature and height. We use NMC values of potential vorticity, interpolated to the latitude, longitude, and time of our aircraft, and for an altitude corresponding to a potential temperature of 440 K. The corresponding pressure altitude is about 18 ± 1 km, varying from about 17 km at mid-latitudes to 19 km at high latitudes (e.g., [*Schoeberl et al.*, 1992]). This is roughly one scale height above the aircraft, and also is close to the altitude of maximum sensitivity of the HF profile to vertical displacement (discussed later). For compactness, we will write values in terms of the potential vorticity unit PVU, defined here as

$$\text{PVU} \equiv 10^{-6} \text{ K m}^2 \text{ kg}^{-1} \text{ s}^{-1}.$$

For adiabatic and frictionless motion, PV is a conserved quantity, and should therefore serve as an indicator of dynamically similar parcels of air, over extended periods of time.

The derived values of subsidence are shown in Fig. 1, plotted as a function of PV. The January, February, and March data are drawn as solid squares, hollow squares, and stars, respectively; the corresponding monthly-average uncertainties in subsidence are 0.016, 0.015, and 0.026, indicated by vertical bars in the key to Fig. 1. The uncertainty in PV is taken to be about 0.6 PVU, which is estimated from the product of a typical rate of change of PV with horizontal distance and a typical measurement scale length. The along-track scale length of about 60 km is the distance traveled by the aircraft during a 4-scan HF measurement; the cross-track scale length of about 45 km is the horizontal distance over which the line of sight rises by about one scale height.

There are several features of the groupings of points in Fig. 1 which deserve mention. First, the scatter in the points appears greater than expected from the stated uncertainties. The evidence suggests that most of this scatter is due to different histories of the air masses, since, for a given narrow range of PV values, there is significantly less scatter among subsidences that are closely adjacent than among ones that are separated by large distances or times. This indicates that PV is not the only parameter of importance in determining subsidence, although, as will be shown below, it is highly significant.

Second, some values of subsidence are likely shifted due to local meteorology, thus increasing the scatter. For example, the lowest January points between about 20 to 30 PVU are from the 19 Jan. crossing of the North Atlantic, during which time a large tropospheric uplift occurred. Since the observed subsidences are weak, this uplift apparently affected at least the lower stratosphere as well.

Third, there are clusters of points near values of 16 and 30 PVU, and relatively fewer points between these clusters. This is due to the extreme spatial steepness of the vortex wall, which tends to lie between values of about 19 and 30 PVU

(see Sec. 4.2). As the aircraft entered or exited the vortex, the wall was usually traversed quickly, although in some cases we did fly roughly parallel to the wall, and this accounts for more points being in the wall region than would be expected from a random sample of geographic points.

Fourth, a series of very low values of PV was encountered in February, when we flew unusually far south, from Maine to south of Puerto Rico. That these points exhibit negative subsidence (i.e., relative uplifting) is not unexpected, because the template HF profile was selected to be typical of more northerly latitudes.

4. Subsidence Trends

We search for trends in the data in Fig. 1 using the following statistical procedure. We bin the data according to the values of 2 parameters, time and potential vorticity. The data from each month are binned in separate groups. Within each month, the data are binned by PV. We use equal-sized bins of width $\Delta PV = 2$ PVU, on centers $PV_i = i$ PVU, where $i = 1-40$. With these choices, adjacent median values are correlated. Bins containing fewer than a threshold number of points are individually widened until they pass the threshold, here set to 6; this helps bridge data-poor regions.

For the n_i points in each bin, the median value \bar{s} of subsidence is found. The uncertainty in each median value is calculated by assuming that the number of samples in each bin can fluctuate statistically by about $\Delta n_i = \sqrt{n_i}$. For an upper limit, we calculate a perturbed median for the case in which the Δn_i points having the smallest value of subsidence are removed from the sample; the lower limit is obtained in a similar fashion. We expect that the uncertainties in the median are overestimated in bins where there are a large number of measurements, but underestimated in bins where there happen to be a few clustered measurements;

as such, the average uncertainty is probably more meaningful than any particular single value. The average uncertainties are $\Delta s_{\text{ave}} = 0.016, 0.025$, and 0.019 for Jan., Feb., and Mar., respectively. The individual median values \bar{s} and uncertainties $\Delta \bar{s}$ are plotted in Fig. 2.

Excluding the February flight to Puerto Rico, all median values have a lower limit of about 13 PVU, reflecting a common starting latitude at Moffett Field. The upper limits on median PV vary from 40 PVU in January to 31 PVU in March; this decrease with time possibly reflects a weakening of the vortex.

The dominant signal in the monthly median subsidence plots is a smooth trend of subsidence with respect to PV. To extract this trend, we construct a third-order polynomial function $s(\text{PV})$, and perform a least-squares fit to the median values \bar{s} , assuming equal weight at each point. These curves are shown superposed on the median values \bar{s} in Fig. 2, and to facilitate comparison, are re-drawn at the same scale in Fig. 3.

In the remainder of this section we examine the data in Figs. 1–3 for clues to the dynamical behavior of the polar vortex, taking advantage of the extended space-time coverage afforded by the DC-8 flights. Conclusions are listed separately for clarity, although there is coupling between them.

4.1. Correlation with PV

From the plots of median subsidence versus PV in Fig. 2, it is clear that there is a strong correlation between these quantities. The correlation is sufficiently good that a smooth curve can be passed through the data points, and the curve taken to represent the data with little loss of information. Quantitatively, the root-mean-square differences between the smooth curve s and the median values \bar{s} are $\Delta s_{\text{rms}} = 0.020, 0.038$, and 0.034 for Jan., Feb., and Mar., respectively. These differences are

about 1.5 and 1.7 times larger than the average uncertainties in the median and individual subsidences, respectively. This underscores the point made earlier that PV is not the sole determinant of subsidence, and that there are other parameters, which we are ignoring here, which probably also play a role. In spite of this caveat concerning the role of secondary factors, Fig. 2 clearly demonstrates that there is a strong correlation between the median subsidence and PV.

4.2. Gradients

In the range $PV \simeq 13\text{--}30$ PVU Fig. 2 shows that subsidence increases dramatically. For smaller values of PV, toward the tropics, we expect that subsidence will become negative, reflecting a general upwelling driven by solar heating; however in this case the appropriate independent variable is likely to be latitude, not potential vorticity. For larger values of PV, Fig. 2 suggests a saturation of subsidence, but there are too few data points here to uphold this speculation.

It is remarkable that the region of maximum slope ds/dPV also coincides with the region of maximum slope of PV with respect to geographic distance dPV/dy_{\perp} . Here y_{\perp} indicates geographic distance in a direction perpendicular to contours of PV. Visual inspection of maps of PV [Tuck *et al.*, 1992] illustrates the well-known fact that the polar vortex is bounded by a sharply-defined “wall” where the contours of constant PV are closely bunched. The product of these gradients is the spatial gradient of subsidence,

$$ds/dy_{\perp} = (ds/dPV) \times (dPV/dy_{\perp}).$$

Since both terms on the right-hand side of this equation are large at the location of the vortex wall (defined here as the region of maximum dPV/dy_{\perp}), it follows that the spatial gradient of subsidence is particularly sharply defined there as well.

Our examination of PV maps for the days of observations reported here shows

that the location of the wall in PV space is the same each month. Measuring between points at the “bottom” and the “top” of the wall, corresponding visually to about the 10 and 90 percent amplitude contours, we find that the outer and inner edges are at

$$PV_{\text{out}} \simeq 19(\pm 1) \text{ PVU}$$

$$PV_{\text{in}} \simeq 30(\pm 2) \text{ PVU},$$

respectively. The width of the wall is thus about

$$\Delta_{\text{wall}} PV \simeq 11(\pm 2) \text{ PVU}.$$

This corresponds to an earth-centered width of

$$\Delta_{\text{wall}} \lambda \simeq 5.7(\pm 0.2)^\circ,$$

and a geographic distance of

$$\Delta_{\text{wall}} y_{\perp} \simeq 640(\pm 120) \text{ km}.$$

Thus the transition region between inside and outside the vortex, or the subsided and non-subsided stratosphere, occupies a narrow geographic band of width about 640 km. By itself, this does not say anything about where descent is taking place. To address this issue, we need to look at the change with time of the descended region, discussed in the next two sections.

4.3. Early winter subsidence

The January trend line shows that by mid-winter there was already a significant degree of subsidence in the vortex. Unfortunately, we do not have any measurements from earlier times, before the vortex was established. In addition to providing a baseline value of subsidence, these also would have been useful in estimating any time delay, or phase lag, between the onset of vorticity and the change of subsidence.

Despite the absence of such data, we may still attempt to estimate the vertical velocity during the first half of the winter season, by assuming that the pre-winter subsidence is zero at the time of the fall equinox. We assign an uncertainty of ± 0.1 to the equinox subsidence. The zero level is indicated by a dashed line in Fig. 3.

We calculate the corresponding vertical displacement by noting that, for a parcel of air, the value of $(1 + s)z$ is conserved, so, taking differentials, we obtain

$$\Delta z = -z\Delta s/(1 + s),$$

where Δz is a small displacement about a mean value z , and Δs is the change in subsidence about a mean value s . The vertical velocity \bar{w}^* is calculated by dividing the displacement by the elapsed time Δt , so

$$\bar{w}^* = \Delta z/\Delta t.$$

In this notation the over-bar indicates a time average, and the superscript asterisk indicates a seasonal fluctuation with respect to the yearly average velocity (here assumed to be zero).

The change in subsidence from September to January is just the difference in the corresponding subsidence curves. The PV range over which one-half or more of the peak subsidence occurs is 22–40 PVU, which we write as 31 ± 9 PVU. In this range, the average change in subsidence is $\Delta s = 0.33 \pm 0.1$, and the time-average mean subsidence is $s = 0.16$. At an altitude of 18 km, which corresponds to the peak sensitivity of HF to descent [Toon *et al.*, 1992], we calculate a vertical displacement $\Delta z_{18} = -5.1(\pm 1.5)$ km. The relevant time interval is $\Delta t = 120$ d, which then allows us to find the vertical velocity $\bar{w}^* = -0.049(\pm 0.015)$ cm/s. These values are collected in Table 1, with the caveat that the initial condition is assumed, not measured.

4.4. Late winter subsidence

The greatest change in subsidence in the January-February interval is in region spanned by $PV \simeq 27(\pm 5)$ PVU, where the time-average subsidence is 0.36, and the increase is 0.12 ± 0.02 . The uncertainty in Δs is estimated from the average rms difference between the polynomials and median value points, which is 0.031, multiplied by $\sqrt{2}$ to account for the difference operation, divided by $\sqrt{n-2}$ where $n \simeq 6$ is the approximate number of independent subsidence points in the overlap region, and the 2 allows for the effective number of degrees of freedom in fitting the median points over a short interval. Following the above procedure, we find a vertical velocity $\bar{w}^* = -0.059(\pm 0.009)$ cm/s.

Likewise, for the period February to March, the greatest increase in subsidence occurred in the interval $PV \simeq 19(\pm 5)$ PVU, where the average subsidence is 0.24, and the increase is 0.07 ± 0.02 . The vertical velocity is $-0.047 \pm .014$ cm/s. These results also are collected in Table 1.

It is interesting to note that the three derived vertical velocities are similar in both early and late winter; their average value is

$$\bar{w}^* = -0.052(\pm 0.013) \text{ cm/s.}$$

This suggests that the air in the descending regions is continuing to cool at about the same rate (even though, as discussed in the next section, the location of the descending air is shifting). The derived vertical velocities for the ranges of PV being considered here are shown in Fig. 4, calculated from the smoothed polynomial curves shown in Fig. 3. At first glance it may seem surprising that the stratosphere is still cooling as late as March, because the spring equinox occurs in that month, and all latitudes up to the pole are in sunlight half of the time. However it may be that what we are seeing here is simply the effect of a time constant in the stratospheric

heating.

Our observed vertical velocities are marginally smaller than those estimated by *Schoeberl et al.* [1992] from calculated cooling rates in the north polar vortex region during the period January 3 to February 10, 1989. At an altitude of 18 km and a latitude around 60°N, coincident with the polar jet and vortex edge, these authors find a zonal average vertical velocity on the order of $\bar{w}^* = -0.07$ cm/s. This is greater than our average measured value, but not at a high level of significance. One might expect that the situation would be reversed, since a zonal average samples many non-vortex locations, and therefore should be a weaker measure.

4.5. Time to flush the stratosphere

From our measured winter-long average value of vertical velocity \bar{w}^* and a nominal value of scale height H of 8 km, we can estimate the characteristic time to flush the stratosphere as

$$T = H/\bar{w}^* \simeq 5.9 \pm 1.5 \text{ month,}$$

at an altitude of about 18 km. This suggests that the air in the stratosphere is replaced relatively slowly, on the order of only once per winter season. The implications of this slow rate of turn-over will be discussed elsewhere.

4.6. Location of descent in PV space

From Fig. 3 and the data in Table 1, the region of maximum descent appears to move outward from the center of the vortex, from a position centered at $PV \simeq 31$ PVU in early winter, to 27 followed by 19 in late winter. In the remainder of this section we discuss the possible mechanisms for this apparent shift of the region of maximum descent.

4.6.1. The simplest picture is one in which the descending air is initially lo-

calized at the highest latitudes, where cooling is initially greatest, and where the highest values of PV are found. Later in winter, as the zone of cooling expands, the region of descent also expands, filling the vortex more fully. Recall that we noted earlier that the vortex wall appears to be essentially fixed in PV-space, at least during the latter half of the winter. Since PV is conserved, it is conceivable that a parcel could sink slowly over a period of months while maintaining its value of PV.

4.6.2. On the other hand, it is also possible to view the data as saying that by mid-January all of the descent had already taken place, and that the shifting trend lines in Fig. 3 simply reflect the decaying vorticity of already-descended air columns. In this view, a given parcel of air has a fixed subsidence throughout the period January to March, but its potential vorticity is slowly decaying. In other words, the January trend line in Fig. 3 is mapped by some transformation of the PV-axis into the February trend line, and thence to the March trend line. Each parcel retains its January subsidence, but simply evolves toward smaller values of PV during the last half of winter. The mechanisms [Brown, 1991, p.322, p.329] for loss of PV are three: horizontal advection, in regions of non-uniform PV; distortion of a parcel, by twisting, stretching, or tilting; and molecular diffusion of PV between parcels. These mechanisms are certainly present during the period of observation. To conserve mass, the volume of stratosphere enclosed by the vortex would have to diminish with time. In possible support of this hypothesis, we note that the peak values of PV encountered during the 3-month period appeared to decrease with time, but this is a weak argument at best, because the result could easily be biased by the small number of samples available. Without a clear indication that these dissipative processes are indeed occurring at a significant rate, we tentatively reject this hypothesis in favor of the simpler one discussed first.

4.6.3. In a third scenario, it might be argued that horizontal diffusion of air

parcels within the vortex accounts for the increased abundance of subsided air at the wall of the vortex. From parcel trajectory calculations *Schoeberl et al.* [1992] find that the diffusion coefficient D is expected to be small, and essentially constant inside the contour 20 PVU, with a value $D \simeq 1.9 \times 10^4 \text{ m}^2/\text{s}$. Then assuming that the diffusion of air parcels across lines of constant PV can be approximated by the simple relation $y_D = \sqrt{2tD}$, we calculate a transverse diffusion distance $y_D \approx 300 \text{ km}$. Since this value is about one-half the thickness of the vortex wall, it is likely that material exchange will take place across the wall on a 1–2 month time period, but that essentially no material can be replenished from the interior of the vortex, since the radius of the interior is much larger than the thickness of the wall. Thus diffusion will likely act to degrade the steepness of the subsidence profile at the outer edge of the vortex, but it cannot account for the large-scale transformation of the median subsidence curves between January and February. Diffusion alone is also unlikely to account for the February to March transformation, because although the apparent shift in PV (and therefore distance) is within a diffusion length, one expects that diffused air from inside the vortex will be diluted with HF-poor air from outside the vortex, and that the apparent subsidence would therefore be halved, at least. But this is not seen in the data, since the March subsidence is essentially the same as, or greater than, the earlier subsidence. It therefore seems that diffusion is too feeble a mechanism to explain the change in shape of the observed subsidence curves during the late winter.

4.6.4. A fourth scenario which might explain the apparent outward shift of subsidence is that the vortex wall is expected to occur at larger radial distances as a function of altitude. In this view the vortex has the shape of a truncated, upward-opening cone. Suppose the vortex evolves throughout the winter from a cone shape with a wide opening angle to one with a narrower opening angle, i.e.,

toward a cylinder. Suppose further that the subsidence is the same at any given altitude inside the cone. Then if nothing else changes, a steepening of the wall would cause the apparent (vertically integrated) subsidence $s(PV)$ to become more sharply defined at the edge of the vortex. This scenario is similar to the first one, but goes further in attributing the apparent outward advance of subsidence to a specific geometrical change, the vertical tilt of the vortex wall.

To summarize this section, the observational evidence suggests that the region of descent appears to move from the center of the vortex toward the outer edge as the winter progresses. The physical mechanism behind this apparent shift remains to be established.

5. Conclusions

From our observations of stratospheric HF in the polar vortex during the winter in 1992, we draw the following conclusions. (1) Subsidence is strongly correlated with potential vorticity. However, there appear to be other factors, including meteorological conditions, which play a lesser role. (2) The gradient of subsidence with respect to potential vorticity is large and approximately constant across the vortex wall, and is small elsewhere. The gradient of subsidence with respect to horizontal distance is dramatically large across the vortex wall. (3) There appears to be substantial descent in the early winter vortex, from the evidence of the observed subsidence in January, and the assumption of zero subsidence at the fall equinox. (4) Descent continues to occur in late winter, with measured vertical velocities similar to that inferred for early winter. The average early and late winter vertical velocity at a representative altitude of 18 km is $0.052(\pm 0.013)$ cm/s. (5) At the measured rate of subsidence, the time required to flush the stratosphere by one scale height is about 6 months. (6) The region of maximum descent appears to

start near the center of the vortex in early winter, and progressively move out to the mid-wall and outer-wall regions in late winter.

Acknowledgements. We thank Jim Changqin Xue for help in numerical calculations, and the NASA Ames DC-8 flight crew for their superb support throughout the AASE-2 campaign. We are grateful to Mark Schoeberl, Leslie Lait, and Paul Neuman for providing NMC curtain file data on temperature profiles and potential vorticity. This work was supported by NASA grant NSG 5175.

References

Brasseur, G., and S. Solomon, *Aeronomy of the middle atmosphere*, D. Reidel Publishing Co., Dordrecht, Holland, 1984.

Brown, R. A., *Fluid mechanics of the atmosphere*, Academic Press, San Diego, CA, 1991.

Johnson, D. G., K. W. Jucks, W. A. Traub, and K. V. Chance, The Smithsonian stratospheric far-infrared spectrometer and data reduction system, submitted to JGR, 1993.

Mankin, W. G., M. T. Coffey, A. Goldman, M. R. Schoeberl, L. R. Lait, and P. A. Newman, Airborne measurements of stratospheric constituents over the Arctic in the winter of 1989, *Geophys. Res. Lett.*, *17*, 473–476, 1990.

Peixoto, J. P., and A. H. Oort, *Physics of climate*, American Institute of Physics, New York, NY, 1992.

Schoeberl, M. R., L. R. Lait, P. A. Newman, and J. E. Rosenfield, The structure of the polar vortex, *J. Geophys. Res.*, *97*, 7859–7882, 1992.

Toon, G. C., C. B. Farmer, P. W. Schaper, L. L. Lowes, R. H. Norton, M. R. Schoeberl, L. R. Lait, and P. A. Newman, Evidence for subsidence in the 1989 Arctic winter stratosphere from airborne infrared composition measurements, *J. Geophys. Res.*, *97*, 7963–7970, 1992.

Traub, W. A., K. V. Chance, D. G. Johnson, and K. W. Jucks, Stratospheric spectroscopy with the far-infrared spectrometer (FIRS-2): Overview and recent results, *SPIE*, *1491*, 298–307, 1991.

Traub, W. A., D. G. Johnson, K. W. Jucks, and K. V. Chance, Upper limit for stratospheric HBr using far-infrared thermal emission spectroscopy, *Geophys. Res.*

Lett., 19, 1651–1654, 1992.

Tuck, A. F., Davies, T., Hovde, S. J., Noguer-Alba, M., Fahey, D. W., Kawa, S. R., Kelly, K. K., Murphy, D. M., Proffitt, M. H., Margitan, J. J., Loewenstein, M., Podolske, J. R., Strahan, S. E., and Chan, K. R., Polar stratospheric cloud processed air and potential vorticity in the Northern Hemisphere lower stratosphere at mid-latitudes during winter, *J. Geophys. Res.*, 97, 7883–7904, 1992.

Addresses

W. A. Traub, K. W. Jucks, D. G. Johnson, and K. V. Chance,
Harvard-Smithsonian Center for Astrophysics,
60 Garden St., Cambridge, MA 02138.

Figure captions

Fig. 1. Stratospheric subsidence, as determined from DC-8 based observations of a far-infrared thermal emission line of HF, for the months of January, February, and March in 1992, plotted against potential vorticity at the 440 K potential temperature level, for the location and time of the aircraft. PVU is defined in the text, and all data are from the Northern Hemisphere (NH). Average uncertainties in individual determinations of s are indicated in the legend.

Fig. 2. (a) Median values of subsidence are shown for January 1992 observations in bins of width $\Delta PV = 2$ PVU, or greater (see text), spaced by intervals of one-half bin (1 PVU). The estimated uncertainty in each median value is indicated by a vertical bar. The smooth curve is that third-order polynomial $s(PV)$ which best fits the median values, in the sense of least-squares. (b) Same, for February 1992. (c) Same, for March 1992.

Fig. 3. Polynomial curves $s(PV)$ for Jan., Feb., and Mar. 1992, reproduced from Fig. 2, showing the trend of stratospheric subsidence with respect to both PV and time. A dashed line indicates that zero subsidence is assumed to occur at about the fall equinox. For reference, the vortex wall lies between PV values of 19 ± 1 PVU and 30 ± 2 PVU during all three months.

Fig. 4. Derived vertical velocities for the periods September 1991 to January 1992, January 1992 to February 1992, and February 1992 to March 1992. Note that the region of maximum descent velocity moves towards regions of lower PV as the season progresses. The calculation of \bar{w}^* is discussed in the text.

TABLE 1. Stratospheric Subsidence from HF Observations

| period | interval | subsiding | change in | descent | vertical |
|-----------|------------|------------|-----------------|-----------------|----------------------|
| | Δt | region | subsidence | Δz_{18} | velocity \bar{w}^* |
| | (days) | (PVU) | Δs | (km) | (cm/sec) |
| 9/91-1/92 | 120 | 31 ± 9 | 0.33 ± 0.10 | -5.1 ± 1.5 | -0.049 ± 0.015 |
| 1/92-2/92 | 32 | 27 ± 5 | 0.12 ± 0.02 | -1.6 ± 0.3 | -0.059 ± 0.009 |
| 2/92-3/92 | 24 | 19 ± 5 | 0.07 ± 0.02 | -1.0 ± 0.3 | -0.047 ± 0.014 |

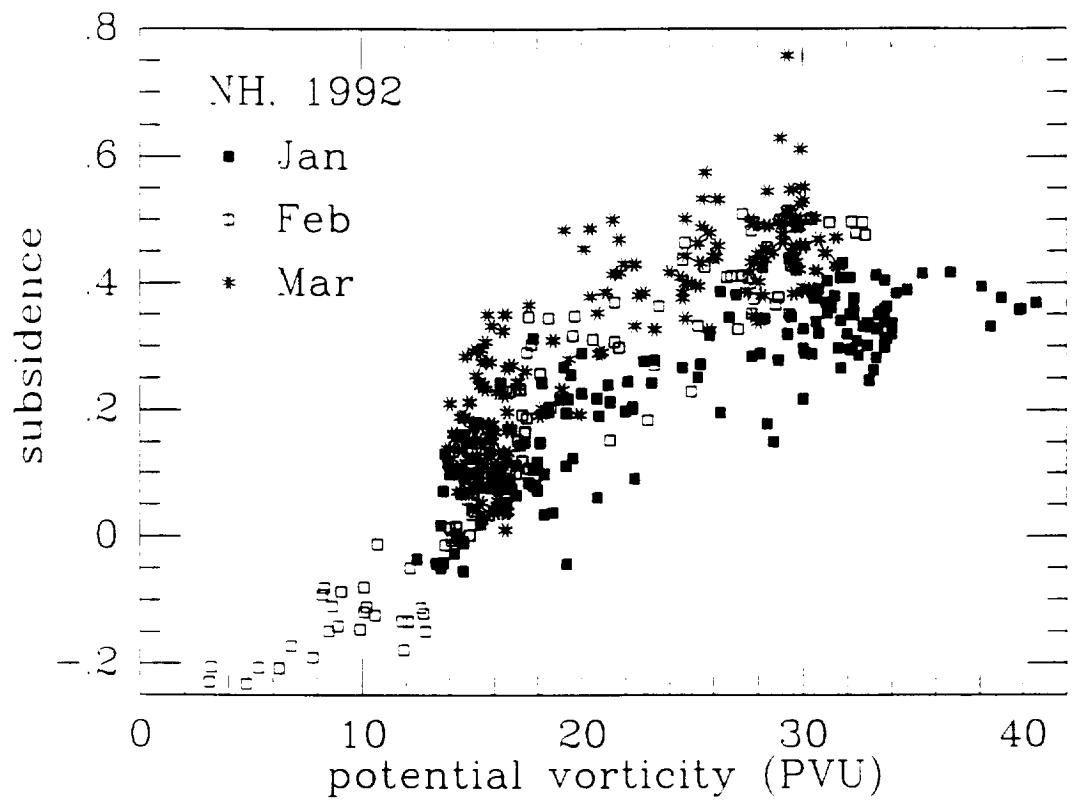


Figure 1

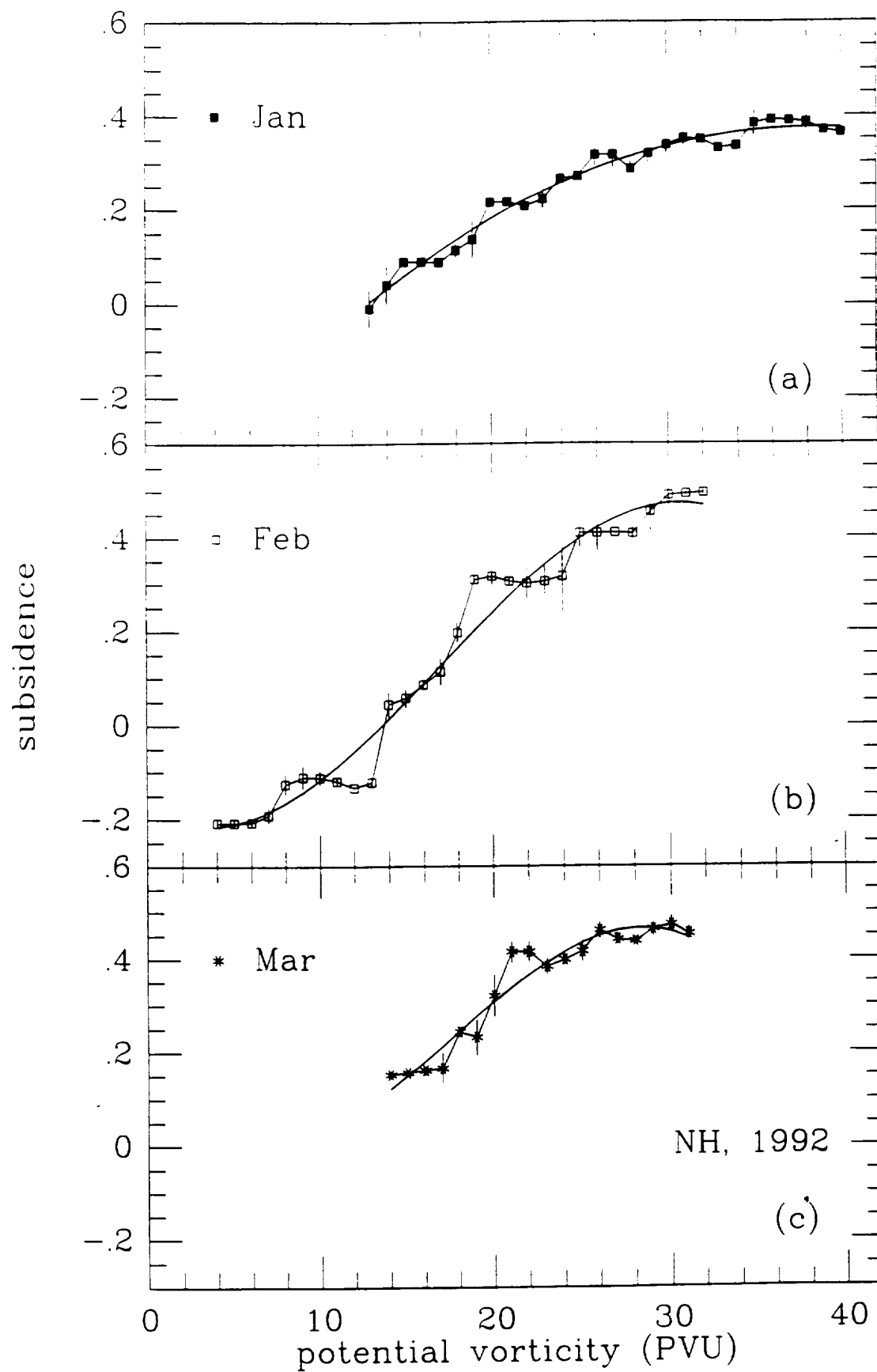


Figure 2

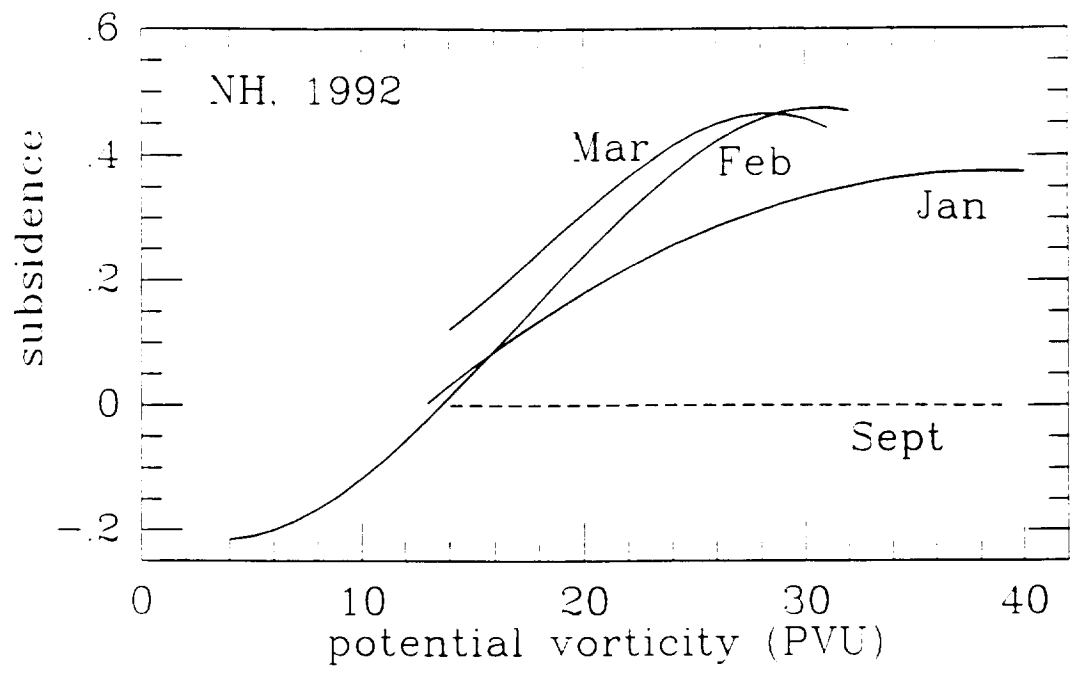


Figure 3

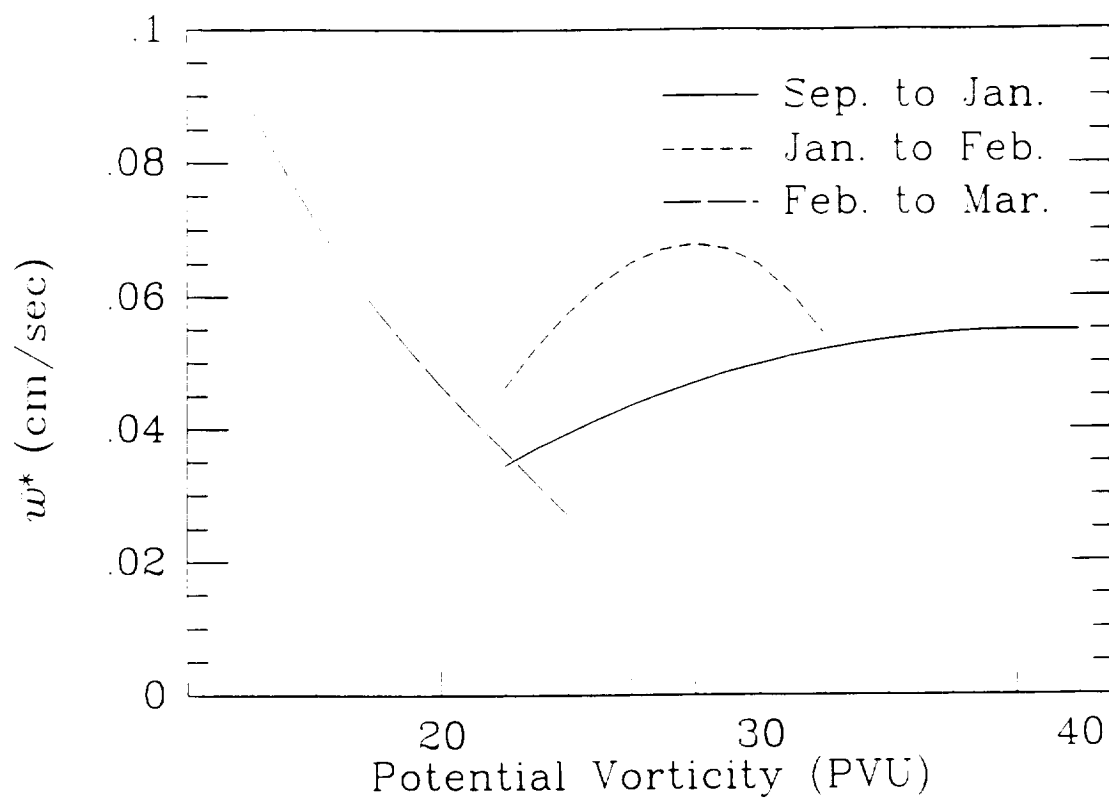


Figure 4

APPENDIX B

The Smithsonian Stratospheric Far-Infrared Spectrometer and Data Reduction System

The Smithsonian Stratospheric Far-Infrared Spectrometer and Data Reduction System

D. G. JOHNSON, K. W. JUCKS, W. A. TRAUB, AND K. V. CHANCE

Harvard-Smithsonian Center for Astrophysics, Cambridge, Massachusetts

The FIRS-2 is a remote-sensing Fourier-transform spectrometer that measures the mid- and far-infrared thermal emission spectrum of the stratosphere from balloon and aircraft platforms. The spectrometer has had eight successful balloon flights from 1987 to 1993, flying at float altitudes of 36–39 km, and collecting 108 hours of mid-latitude stratospheric limb spectra. The spectrometer also flew on a NASA DC-8 aircraft, as part of the second Airborne Arctic Stratospheric Expedition (AASE-II), collecting 140 hours of overhead spectra at latitudes ranging from the equator to the North Pole. We present here a brief description of the instrument, a discussion of data reduction procedures, an estimation of both random and systematic errors, an outline of the procedure for retrieving mixing ratio profiles, and an explanation of the method of deriving temperature and pressure from the far- and mid-infrared spectra.

1. INTRODUCTION

The far-infrared spectrometer FIRS-2 was designed and built at the Smithsonian Astrophysical Observatory for the purpose of measuring molecular abundances in the earth's stratosphere. It is the successor to the FIRS-1 [Traub *et al.*, 1982], which had 6 productive balloon flights in the years 1979 to 1983, but which was destroyed by a free-fall in 1983. On a balloon platform, FIRS-2 measures the thermal emission spectra of a number of species important in stratospheric chemistry. The far-infrared channel ($80\text{--}200\text{ cm}^{-1}$) contains useful spectral lines of 12 species: H_2O , O_2 , O_3 , NO_2 , HF , HBr , HCl , HOCl , HO_2 , OH , H_2O_2 , and $\text{O}(^3\text{P})$; the mid-infrared channel ($350\text{--}700\text{ cm}^{-1}$) contains lines of 3 additional species: CO_2 (which yields pressure and temperature), N_2O , and HNO_3 . The total list includes 15 species, which grows to 21 if all isotopomers currently measured as separate species are included. On the DC-8 aircraft platform, the FIRS-2 measures 6 species: H_2O , O_2 , O_3 , HF , HCl , and HNO_3 , plus two isotopomers.

We derive atmospheric temperatures from an analysis of temperature-sensitive CO_2 lines, and check telescope pointing angles by analyzing a separate set of CO_2 lines which are sensitive to

column density. We measure mixing ratio profiles of all other molecular species by fitting calculated spectra to the observed spectra, using the derived temperatures and pressures.

In this paper we discuss many of the unique aspects of the FIRS-2 instrument and data analysis procedure, emphasizing our efforts to achieve high degrees of accuracy and precision in the derived stratospheric profiles. A previous discussion of the instrument and its uses is found in *Traub et al.* [1991].

2. MEASURING INFRARED EMISSION SPECTRA

The balloon flight instrument is composed of the Fourier transform spectrometer itself, a telescope, scan platform, infrared detectors, electronics, and telemetry transmitters and receivers. During a flight the interferograms and engineering data are telemetered to the ground and recorded on an optical disk or an 8 mm digital tape. Later the interferograms are extracted, transformed, phase corrected, and normalized.

The DC-8 flight instrument uses the same spectrometer as on the balloon, but the telescope and scan platform are different. We also replace the telemetry command and data links by hard-wired connections, and we isolate the instrument from vibrations of the aircraft frame by a pneumatic support system.

2.1. SPECTROMETER

The spectrometer collimating and imaging mirrors are 10.1 cm in diameter and have focal lengths of 58.0 cm. The nominal beam diameter is 7.6 cm. We use hollow corner cube retroreflectors which have a hexagonal aperture of outside diameter 17.6 cm. There are two input and two output beams with separations between their axes of 7.6 cm. One input is coupled to the sky radiation, and the second is coupled to a liquid nitrogen cooled blackbody source. Both outputs are coupled to detectors. The beamsplitter is a $12\text{ }\mu\text{m}$ -thick uncoated Mylar sheet stretched over an optically flat glass ring. One corner cube is fixed, while the other scans over path differences of -1.2 to $+120$ cm. The short two-sided part of the interferogram provides low resolution phase information, while the long one-sided interferogram gives a resolution element of $1/2L$ (unapodized), where L is the maximum optical path difference (opd). For $L = 120$ cm, the resolution element is 0.004 cm^{-1} .

The optics preceding the detector dewar are at ambient temperature, and are oversized. In the dewar there is a 4-K aperture stop and field stop for each beam; the aperture stop blocks thermal background radiation from the instrument itself (except for thermal emission from the mirrors), and the field stop limits the field of view (FOV) on the sky as well as preventing self-apodization at the highest frequency sampled by each detector. At the spectrometer input and output ports, where the field is imaged, the nominal cold beam speed is $f/9$, and the cold field diameter is 0.67 cm for the far-infrared channel and 0.47 cm for the mid-infrared channel. These values give a system etendue or throughput of $3.4 \times 10^{-3}\text{ cm}^2\text{ str}$ and $1.7 \times 10^{-3}\text{ cm}^2\text{ str}$, respectively.

We use an HP model 5701 HeNe laser in an optical interferometer to measure the scan mirror position and control its velocity. The mirror is constrained to move along a parallel set of rails and is driven by a lead screw. We enclose the entire optical system in a vacuum chamber, except for the laser tube which is held at one atmosphere. On balloon platforms we scan the mirror at 12,000 HeNe fringes per second, the scan rate being constrained by our telemetry bandwidth. On the DC-8

we scanned the mirror at a higher rate, 60,000 fringes per second, in order to increase the time resolution of our measurements, and to shift the modulated infrared frequency band above aircraft vibration frequencies. In this case, the scan rate is limited by the performance of the mirror servo system. The average acquisition time per interferogram is 180 seconds in the balloon configuration and 39 seconds on the DC-8, including overhead.

2.2. TELESCOPES

For operation from balloon platforms we couple the spectrometer input to a small off-axis reflecting telescope, which has a 20 cm diameter spherical primary mirror with a focal length of 175 cm. The FOV of the far-infrared detector is 0.22° , which at a typical elevation angle of -3° corresponds to 1.3 km at the tangent altitude, or about one quarter of an atmospheric scale height. During balloon flights we can control the telescope azimuth to an accuracy of $\pm 2^\circ$ by orienting the gondola with a magnetometer-controlled servo system designed and built at Jet Propulsion Laboratory. We independently measure the azimuth with a magnetometer made by KVH Industries, Inc., which automatically compensates for any additional fixed magnetic field from the gondola. We control the elevation angle to $\pm 0.02^\circ$ by referencing the telescope elevation to a single axis stabilized platform which uses a gyroscope as a short term inertial reference and an inclinometer to correct for offsets and long term drift in the gyroscope [Coyle, *et al.*, 1986; Traub *et al.*, 1986].

While operating the spectrometer on board the NASA DC-8 observations are made from cruising altitudes near the base of the stratosphere, typically 11 ± 1 km. We only obtain useful data while viewing above the horizon because tropospheric water vapor and carbon dioxide obscure much of the spectral regions of interest for negative angles. Since the column density is much less dependent on the size of the FOV for positive elevation angles than is the case for negative elevation angles, we are able to replace the telescope with a compact scan platform consisting of a small flat

scan mirror combined with a stationary collimating mirror with a focal length of 58 cm. giving the far-infrared detector a 0.66° field of view. The azimuth for each observation is determined entirely by the aircraft heading. The elevation is measured with respect to the aircraft frame, and servo-corrected for the aircraft roll as determined by the inertial navigation system. The pointing accuracy is limited by the accuracy of the aircraft roll information, which we estimate to be about $\pm 0.1^\circ$.

2.3. DETECTORS

Both spectrometer outputs are coupled to a liquid helium dewar which houses the detectors and the first amplifier stage. The dewar is configured to allow splitting each spectrometer output, giving a maximum of four output channels. The spectrometer has flown with three far-infrared and one mid-infrared channel, but currently just one far-infrared and one mid-infrared channel are used. We use a Ge:Ga photoconductor with a stacked quartz-CaF blocking filter for far-infrared detection, and a Ge:Cu photoconductor with a Ge-substrate low pass interference filter for detecting mid-infrared radiation. Cooled FET source followers on all the photoconductors provide a low impedance output from the dewar.

Detector outputs are sampled and digitized as the mirror is scanned at a constant velocity. The sample interval is determined by counting fringes from the HeNe interferometer which controls the scan mirror. The far-infrared channel is sampled every 30 fringes and the mid-infrared channel is sampled every 10 fringes, providing Nyquist cutoffs at 263.3 cm^{-1} and 790 cm^{-1} respectively. The audio bandpass is determined by low pass Bessel filters, and the optical bandpass is set by the optical blocking filters; together, these filters essentially eliminate high frequency contributions which could otherwise be aliased into our bands.

2.4. FOURIER TRANSFORMATION AND PHASE DETERMINATION

Starting with the observed interferogram, we estimate the location of the zero-path-difference (ZPD) point, and we multiply the local two-sided part of the interferogram by a linear ramp function so as to equally weight path differences sampled twice (two-sided part) and path differences sampled once (long one-sided part). The short side of the interferogram is zero-padded so that each side contains the same number (2^n) of points, and a Fourier transform is calculated, giving 2^n complex spectral points. The problem is to extract a real spectrum from the complex one. This can be stated in terms of finding the phase angle between the complex input vector and real output vector at each point in the spectrum. We perform the phase determination in one of two ways, depending on whether or not the spectrum contains spectral lines.

We assume that the phase function $\phi(\sigma)$ has the form

$$\phi(\sigma) = \phi(0) + 2\pi\sigma\delta x + \epsilon(\sigma), \quad (1)$$

where σ is wavenumber (cm^{-1}), $\phi(0)$ is 0 or π depending on whether the interferogram peak at ZPD is positive or negative, δx is the error in determining the ZPD point in the interferogram before transforming, and $\epsilon(\sigma)$ is a correction term.

In an ideal spectrometer the phase $\phi(\sigma)$ is strictly linear, and $\epsilon(\sigma)$ is identically zero. This is also true for the case of an absorbing beamsplitter in the limit when either the beamsplitter has zero physical thickness or when the beamsplitter is a uniform slab with a complex index of refraction. However, if the beamsplitter is asymmetric, i.e., if the complex index of refraction as a function of depth is not a symmetric function of distance from the physical center of the slab, then $\epsilon(\sigma)$ may be non-zero. In our case, the beamsplitter is an uncoated sheet of Mylar, with an optical thickness on the order of a wavelength. *A priori*, one might expect this sheet to be uniform. However, as discussed below, since we observe $\epsilon(\sigma)$ to be non-zero, particularly in the areas where Mylar has absorption features, we hypothesize that the beamsplitter is slightly asymmetric. In the

following paragraphs, we discuss the methods we use to find, first, the linear terms $\phi(0)$ and δx for each spectrum, and second, the non-linear correction term $\epsilon(\sigma)$.

2.4.1. LINEAR PHASE TERMS FOR CONTINUUM SPECTRA

For spectra of continuum sources, we first calculate a low resolution phase function from the phase of the complex transform of the short two-sided part of the interferogram. We subtract the pre-determined correction term $\epsilon(\sigma)$ (see below) from the phase and then fit a linear function to the remainder over spectral regions where the detector and spectrometer are sensitive, in order to determine δx and $\phi(0)$. We then phase correct the full resolution spectrum using Eq. (1).

2.4.2. LINEAR PHASE TERMS FOR LINE SPECTRA

In emission line spectra, particularly those taken at high elevation angles, the continuum phase derived from the short two-sided transform is dominated by a background component which we observe to have a phase function different from that of the sky signal. The instrumental line shape is very sensitive to the phase, and small errors in phase produce a pronounced asymmetry in the line shape for a one-sided transform. For example, in the case of a spectrum consisting of a single unresolved line centered at σ_0 , the interferogram $F(x)$ can be expressed as $a \cos(2\pi x \sigma_0 + \phi)$ where x is the instantaneous opd. Transforming a single sided interferogram gives

$$\begin{aligned}\tilde{F}(\sigma) &= \frac{1}{L} \int_0^L F(x) e^{i2\pi x \sigma} dx \\ &= \frac{ae^{-i\phi}}{2} \left[\frac{\sin \alpha}{\alpha} + i \frac{(1 - \cos \alpha)}{\alpha} \right],\end{aligned}\tag{2}$$

where L is the maximum opd, $\alpha \equiv 2\pi L(\sigma - \sigma_0)$, and we have dropped the terms containing $(\sigma + \sigma_0)$. Assuming that ϕ is known, multiplying \tilde{F} in Eq. (2) by $e^{i\phi}$ and taking the real part leaves the term $\sin \alpha / \alpha$, which is just the transform of the sampling function, as expected. However, if the phase is incorrectly determined an antisymmetric error term is introduced which broadens the emission lines, produces asymmetry in the line shape, and shifts the position of the line peak. Turning this

problem around, we determine ϕ for any selected emission line by finding the phase which produces a symmetric line shape. We measure the line phase for about fifty lines distributed throughout the spectrum, fit a linear function to the set of measured phases (after subtracting the correction term) to determine δx and $\phi(0)$, and then phase correct the full resolution spectrum using Eq. (1) as for continuum spectra.

2.4.3. NON-LINEAR PHASE TERM

The problem of determining the non-linear phase term $\epsilon(\sigma)$ is complicated by the fact that each spectrum contains a background component with a phase different from that of the sky signal. This background must be subtracted before $\epsilon(\sigma)$ can be determined. A more complete discussion of this problem is given by *Revercomb et al.* [1988]. Initially, we assume that $\epsilon(\sigma) = 0$. Next, we determine δx and $\phi(0)$ for a balloon spectrum taken at a high elevation angle by symmetrizing lines in the full resolution transform and then use Eq. (1) to correct the complex transform of the short two-sided part of the same interferogram for the ZPD error. We then take the complex transform of the short two-sided part of a warm blackbody scan, correct for the ZPD error by fitting a linear phase function in sensitive regions as described in Sec. 2.4.1 (still assuming that $\epsilon(\sigma) = 0$), and subtract the complex, low resolution, high elevation angle spectrum from the result. Since both spectra have been corrected for the ZPD error, the background cancels out when we calculate the difference. The resulting complex spectrum, blackbody minus sky, consists of radiation from outside the instrument only. The phase of the difference spectrum gives $\epsilon(\sigma)$. The correction term appears to be constant in time, so we have averaged a number of measurements of $\epsilon(\sigma)$ together and use the averaged function to determine the phase for all other spectra. In Fig. 1 we compare $\epsilon(q)$ to some Mylar absorption data, showing the close relationship between absorption features and phase deviations. This suggests that the phenomena are related; however a complete investigation of the relationship is beyond the scope of this paper.

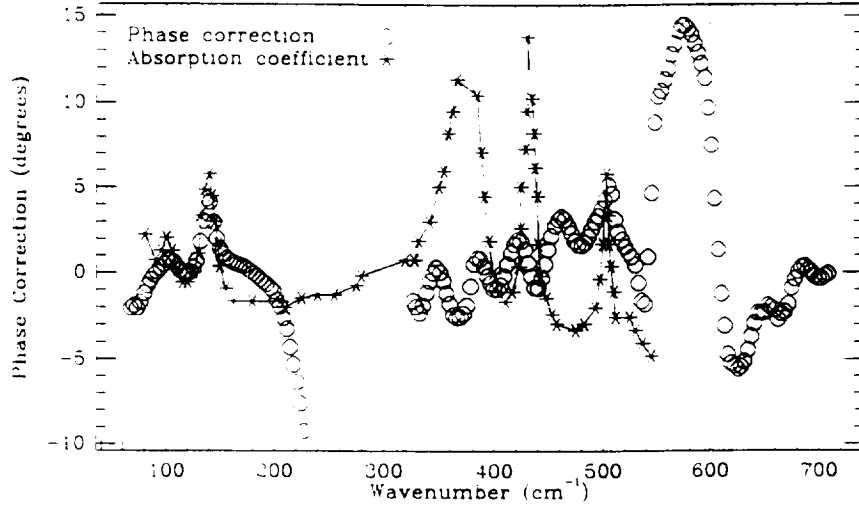


Fig. 1. A comparison of the non-linear phase correction term $\epsilon(\sigma)$ (open circles) and the Mylar absorption spectrum (stars, from *Ciarpailini* [1992]). The scale for the Mylar absorption is arbitrary. Zeros in the beamsplitter efficiency function occur at 0, 260, and 520 cm^{-1} .

2.5. INTENSITY CALIBRATION

We determine the gain and offset of the spectral intensity as a function of wavenumber by reference to the spectra of two blackbodies of known temperature. For convenience we normalize the intensity scale by the intensity of a blackbody at a reference temperature of $T_{ref} = 277 \text{ K}$, a typical temperature for our warm calibration source. If $V_s(\sigma)$, $V_w(\sigma)$, and $V_c(\sigma)$ denote uncalibrated phase corrected spectra of the sky, warm blackbody source, and cold blackbody source respectively. T_w and T_c are the temperatures of the warm and cold sources, $B(\sigma, T)$ is the intensity of a blackbody radiator at a frequency σ and temperature T , and $N_s(\sigma)$ is the intensity of the sky radiation normalized to T_{ref} , then

$$N_s(\sigma) = \frac{V_s(\sigma) - V_c(\sigma)}{V_w(\sigma) - V_c(\sigma)} \times \frac{B(\sigma, T_w) - B(\sigma, T_c)}{B(\sigma, T_{ref})} + \frac{B(\sigma, T_c)}{B(\sigma, T_{ref})}. \quad (3)$$

For the DC-8 flight series the warm source was electrically heated and the cold source was cooled with a thermoelectric cooler to give a temperature difference of 45 K to 60 K. For balloon flights we allow the warm source to equilibrate with the ambient temperature, and we derive the cold spectrum by clipping lines from a high elevation angle (30°) spectrum. In this case the continuum

emission is due to instrumental background so that T_c is effectively zero, which simplifies Eq. (3):

$$N_s(\sigma) = \frac{V_s(\sigma) - V_c(\sigma)}{V_w(\sigma) - V_c(\sigma)} \times \frac{B(\sigma, T_w)}{B(\sigma, T_{ref})} . \quad (4)$$

During observing runs we include a pair of calibration spectra in each sequence of pointing angles, which works out to once every 45 minutes for balloon platforms and once every 12 minutes on the DC-8. In both cases, we smooth the calibration spectra V_w and V_c to a resolution of 0.5 cm^{-1} before normalization. We estimate the gain and offset as a function of time by using a simple two point interpolation for times between calibrations.

2.6. FREQUENCY CALIBRATION

The frequency interval between adjacent points in our transformed spectra is given by

$$\Delta\sigma = \frac{1}{2Nm\lambda_0}(1 + \epsilon_c) , \quad (5)$$

where $N = 2^n$ is the number of points in the full resolution transform, m is the number of HeNe fringes between sample points, and λ_0 is the vacuum wavelength of the HeNe laser used in the mirror servo system. The correction term ϵ_c incorporates corrections arising from the finite size of the entrance aperture (the dominant term), imperfect co-alignment between the laser beam and the direction of mirror travel, and the index of refraction of residual gas in the spectrometer tank. We determine the correction term empirically by measuring the precise positions of a number of well characterised lines in our spectra, using HCl and HF in the far-infrared and CO₂ in the mid-infrared. A typical correction term is $\epsilon_c \approx 1.0 \pm 0.2 \times 10^{-5}$, which is equivalent to a shift of about $0.25 \Delta\sigma$ at 100 cm^{-1} .

3. CALCULATING INFRARED EMISSION SPECTRA

Our program for calculating atmospheric emission is based on the one described in *Traub and Stier* [1976]. To calculate a synthetic spectrum, we divide the atmosphere into a number of thin homogeneous spherical shells, compute the optical depth $\tau(\sigma)$ within each shell, and propagate thermal radiation from the far side of the atmosphere to the observer along the line of sight, including the effects of refraction. Specifically, in each shell we attenuate the incoming radiation by the factor $e^{-\tau}$, and we add the thermally emitted radiation $Be^{-\tau}$, where B is the blackbody source function at the temperature of the shell. To reduce calculation time when computing the optical depth array, we typically include only those lines which contribute a central optical depth of at least 5×10^{-4} in each layer, and we extend the wings of each line to the edge of the calculation window or to an optical depth of 5×10^{-5} .

We use the H-C-G (van der Hulst, Curtis, Godson) approximation [*Goody and Yung*, 1989] to compute the optical depth, defining the effective temperature and pressure (T_{eff} and P_{eff}) in each shell to be the air-mass-weighted temperature and pressure averaged along the line of sight. The choice of the best temperature for the source function is complicated by the fact that it depends on the optical depth and temperature gradient within the shell. We have chosen to use T_{eff} for the source temperature when the optical depth is less than one, and for larger optical depths we use the temperature at the point along the line of sight where the optical depth within the shell reaches one (assuming that the temperature varies linearly with altitude between the altitude where the pressure equals the effective pressure and the altitude of the shell boundary).

If we are viewing towards empty space, then the source strength outside the atmosphere is assumed to be zero, and the computed spectrum will be dominated by emission lines. If we wish to model the case of atmospheric absorption of light from the center of the solar disk (which is the mode of operation of several other types of spectrometers), then we set the external source equal

to a 6.110 K blackbody.

3.1. INITIAL MODEL ATMOSPHERE

The initial model atmosphere consists of our best *a priori* estimates for temperature, pressure, and molecular composition as a function of altitude and time. For balloon flights we average together measurements of temperature as a function of pressure made by radiosondes launched from stations near the balloon at the time of the flight, ± 1 day. We assume that the atmosphere is in hydrostatic equilibrium and calculate temperature and pressure as a function of altitude up to the maximum altitude reached by the radiosondes, about 35 km. We extrapolate this model up to 100 km using the U. S. 1976 Standard Atmosphere. We derive the initial volume mixing ratio (*vmr*) profiles for most molecules from the results of a one-dimensional photochemical model (Mark Allen, private communication, 1991). We use the 1976 Standard Atmosphere profile for O₃, and a combination of the 1976 Standard Atmosphere and measured trends to estimate the initial profiles for HF, HCl, and CO₂. For the DC-8 flights profiles of temperature and pressure as a function of time and altitude along the flight track were provided by the National Meteorology Center. We derive the initial mixing ratio profiles from mid-latitude ATMOS measurements, adjusting some profiles to extrapolate observed trends from the year of the measurement to 1992 (G. Toon, private communication, 1992).

Our discrete model atmosphere consists of a number of homogeneous spherical shells, where within each shell the values of pressure, temperature, and *vmr* are independent of altitude. For ray-tracing calculations, the shells are made to be so thin as to be essentially continuous; we use $1.0 + 2.88 \times 10^{-4} (273.15/T) (P/1013.25)$ for the far-infrared index of refraction, where T is temperature (K) and P is pressure (mb). For synthetic spectrum calculations, most of the shells are about one-half scale height in thickness, and the boundaries are determined by the observing ray paths as described below.

The continuous model atmosphere $\{P(z), T(z)\}$ is discretized by defining an equivalent set of homogeneous, spherical shells, also called layers here. The upper and lower altitudes of the i -th layer are $Z(i)$ and $Z(i + 1)$. These layer boundaries depend on the viewing geometry, the observation altitude, and the species to be measured. In all cases, we fix one boundary at the spectrometer altitude. We set the lower boundaries of layers below the spectrometer equal to the tangent heights for the set of downward looking rays, using a refracted ray propagation path in the essentially continuous model atmosphere. For balloon spectra, we divide the overhead atmosphere into two layers of equal air mass, except when modeling the emission of species having very steep concentration gradients, such as OH, HO₂, and O(³P). In these cases, we divide the overhead column into seven layers. When calculating DC-8 spectra we divide the atmosphere into nine overhead layers.

Once the layer boundaries are determined, we again follow each refracted ray through the essentially continuous model atmosphere and calculate: (a) the line-of-sight column density of air $N(i, j)$ (molecules cm⁻²) within each layer; (b) the effective pressure $P_{\text{eff}}(i, j)$ within each layer, defined as the air-mass weighted pressure along the line of sight; (c) the effective altitude $Z_{\text{eff}}(i, j)$, defined as the altitude at which $P[Z_{\text{eff}}(i, j)] = P_{\text{eff}}(i, j)$; and (d) the effective temperature $T_{\text{eff}}(i, j)$, defined in the same way as the effective pressure; where i and j are the layer and ray indices respectively. We then replace the continuous model atmosphere $\{P(z), T(z)\}$ with a discrete set of homogeneous layers $\{Z(i), Z(i + 1), Z_{\text{eff}}(i, j), N(i, j), P_{\text{eff}}(i, j), T_{\text{eff}}(i, j)\}$. For greatest accuracy, we retain the double-subscripted quantities in all calculations, but when reporting results we select only the value determined by the most sensitive ray j passing through a given layer i , which reduces the set to a single vector $\{Z_{\text{eff}}(i), P_{\text{eff}}(i), T_{\text{eff}}(i)\}$.

3.2. MOLECULAR PARAMETERS

We maintain our own listing of molecular line parameters, the current version of which is SAO92 [Chance *et al.*, 1993]. We use the line parameters from the HITRAN92 catalog [Rothman *et al.*, 1992] for H_2^{16}O (several transitions which interfere with the retrieval of other molecules have been shifted to reflect their apparent position in stratospheric spectra), H_2^{17}O , H_2^{18}O , HDO (lines above 100.4901 cm^{-1} are from HITRAN82), CO_2 , $^{16}\text{O}^{16}\text{O}^{16}\text{O}$, $^{18}\text{O}^{16}\text{O}^{16}\text{O}$, $^{16}\text{O}^{18}\text{O}^{16}\text{O}$, O_3 hot bands, N_2O (lines strengths for the ν_2 fundamental transitions are from J. W. C. Johns, private communication, 1993), CH_4 , NO , SO_2 , NH_3 , HNO_3 , HI , ClO , OCS , H_2CO , N_2 , HCN , CH_3Cl , C_2H_2 , C_2H_6 , and PH_3 . For CO , the positions for the $^{12}\text{C}^{16}\text{O}$ fundamental are from TuFIR work [Varberg and Evenson, 1992], with all other information taken from the HITRAN92 catalog. For oxygen, the $^{16}\text{O}^{16}\text{O}$ and $^{16}\text{O}^{18}\text{O}$ intensities and positions from $10\text{--}100\text{ cm}^{-1}$ are from the July 1992 release of the JPL submillimeter (JPLSMM) line catalog [Poynter and Pickett, 1984], and all parameters for $^{16}\text{O}^{17}\text{O}$ and remaining parameters for the first two isotopic variants are taken from HITRAN92. For NO_2 , the strengths and positions for lines between from 10 and 200 cm^{-1} are from JPLSMM, and the strengths and positions for other lines and all other parameters are from HITRAN92. The OH line widths, including the temperature dependence, are derived from TuFIR measurements of the line at 118.455 cm^{-1} [Chance *et al.*, 1991a]; the positions for all other OH lines are from JPLSMM. HF line positions up to R_4 , HCl positions up to R_{11} , and HBr fundamental positions below 200 cm^{-1} are all from TuFIR measurements [Nolt *et al.*, 1987; Di Lonardo *et al.*, 1991]. The line widths for HF and HCl are from Pine and Looney [1987], and the strengths for the TuFIR-measured lines of HF, HCl, and HBr are from calculations done at SAO, using the dipole moment measurements of Muentert and Klemperer [1970], Kaiser [1970], and Dabbousi *et al.* [1973], respectively; other parameters and all hot band parameters are from HITRAN92. The positions for the strongest lines of HOCl are calculated from Carlotti *et al.* [1990], and other parameters and

line positions are from HITRAN92. For H_2O_2 we have included only the $^R\text{Q}_4$ and $^R\text{Q}_5$ Q-branch lines, with positions calculated from *Masset et al.* [1988] (J. M. Flaud, private communication, 1991), strengths calculated at SAO, and dipole moment from *Cohen and Pickett* [1981]. HO_2 lines in the far-infrared use TuFIR measured positions (K. Chance, to be published), and strengths and additional positions from calculations at JPL [*Poynter and Pickett*, 1984]. Finally, parameters for $^{17}\text{O}^{16}\text{O}^{16}\text{O}$, $^{16}\text{O}^{17}\text{O}^{16}\text{O}$, and $\text{O}_2(^1\Delta)$ are from JPLSMM, and line positions for $\text{O}(^3\text{P})$ are determined by *Watson et al.* [1984].

3.3. INSTRUMENT FUNCTION

The theoretical instrument function $G(\sigma)$ can be selected to be either a discrete delta-function (G_1), Gaussian (G_2), Lorentz (G_3), sinc (G_4), sinc-squared (G_5), sinc-Hamming (G_6), or sinc-von Hann (G_7), with any value of full width at half maximum (FWHM), except for G_1 .

The functions G_4 – G_7 are based on a generalized sinc function $g(\alpha)$, defined here as the real part of the complex instrument function $\tilde{F}(\sigma)$ defined by Eq. 2, dropping the constant factor $a/2$:

$$g(\alpha) = \cos \phi \frac{\sin \alpha}{\alpha} + \sin \phi \left(\frac{1 - \cos \alpha}{\alpha} \right) . \quad (6)$$

As before, $\alpha = 2\pi L(\sigma - \sigma_0)$, where L is the maximum opd in the observed interferogram. The phase angle ϕ represents the phase error discussed earlier. The function $g(\alpha)$ thus models the effects of interferogram truncation and the phase recovery error. In addition, we model the effect of a finite diameter circular aperture by numerically convolving $g(\alpha)$ with a square function of width w (FWHM), giving

$$G_4(\alpha) = \frac{1}{w} \int_{\alpha-w/2}^{\alpha+w/2} g(\alpha') d\alpha' , \quad (7)$$

where $w = (\pi\sigma_0 d^2)/(8F^2\delta\sigma)$, d is the diameter of the detector aperture (0.67 cm for the far-infrared channel) and F is the focal length of the spectrometer imaging mirror (58.0 cm) [*Bell*, 1972]. Additional broadening factors, such as imperfections in the mirrors, misalignment of the beamsplitter, or vibrations in the carriage, can be modelled by increasing the value of d .

A linear taper of the interferogram before transformation gives the instrument function G_5 :

$$G_5(\alpha) = \frac{1}{w} \int_{\alpha-w/2}^{\alpha+w/2} \left[\cos \phi \left(\frac{1 - \cos \alpha'}{\alpha'^2} \right) + \sin \phi \left(\frac{\alpha' - \sin \alpha'}{\alpha'^2} \right) \right] d\alpha' . \quad (8)$$

Note that the coefficient of $\cos \phi$ can also be written as $0.5(\sin 0.5\alpha/0.5\alpha)^2$, so that the integrand could be called a generalized sinc-squared function.

Two varieties of apodization which we find to be useful are Hamming and von Hann, which lead to the instrument functions G_6 and G_7 :

$$G_6(\alpha) = 0.23G_4(\alpha - \pi) + 0.54G_4(\alpha) + 0.23G_4(\alpha + \pi) . \quad (9)$$

$$G_7(\alpha) = 0.25G_4(\alpha - \pi) + 0.50G_4(\alpha) + 0.25G_4(\alpha + \pi) . \quad (10)$$

In the limits $w \rightarrow 0$ and $\phi = 0$ the first side lobes of the generalized sinc, sinc-squared, sinc-Hamming, and sinc-von Hann functions are -21.0% , $+4.5\%$, -0.6% , and -2.7% , respectively; the wings are carried out to 500, 10, 9, and 8 zero-crossings on either side of the central maximum, so the truncated side lobe amplitudes are less than 0.6% , 0.1% , 0.5% , and 0.1% , respectively. In the extreme wings of $G(\sigma)$ the last 10% of points are linearly tapered to zero, to eliminate any sharp discontinuities. Once $G(\sigma)$ has been calculated, it is renormalized to give a total area of one.

When either sinc-Hamming or sinc-von Hann apodizing functions are used, the observed spectra can be apodized with the same type of function simply by calculating running 3-point weighted sums using the weights (0.23, 0.54, 0.23) or (0.25, 0.50, 0.25), respectively. We typically use the von Hann apodization function because it minimizes the influence of lines outside the calculation window.

When calculating the theoretical spectrum and instrument function, we typically use a fine grid size of 0.0002 cm^{-1} or less. To allow for the wings of neighboring features, we usually extend the calculation for 2 cm^{-1} on either side of the spectral window. The convolved spectrum (theoretical * instrument) is computed on an output grid which exactly matches that of the observed spectrum,

i.e., $\Delta\sigma \simeq 0.004 \text{ cm}^{-1}$; this is also the grid on which numerical comparisons are made between observed and theoretical spectra. for least-squares fitting, for example. For graphical presentation, both the theoretical and experimental spectra are interpolated onto a 10-times finer grid, $\Delta\sigma/10$, using the interpolation function $\sin(\pi\sigma/\Delta\sigma)/(\pi\sigma/\Delta\sigma)$; this function reproduces the original points on the $\Delta\sigma$ grid and provides a smooth connection between these points consistent with the band-limited nature of the observed spectrum.

4. RETRIEVALS FROM BALLOON SPECTRA

We use a non-linear least-squares (NLLS) program to vary selected parameters in the initial model atmosphere until the mean-square difference between the observed and model spectrum in the window region is minimized. The NLLS program (Gaushaus) is a standard Levenberg-Marquardt algorithm (see, for example, *Press et al.* [1986]) which calculates an output parameter vector, uncertainty vector, and a parameter correlation matrix. The number of degrees of freedom used to estimate the uncertainty vector is $n - p$, where n is the width of the spectral window in units of the theoretical instrument function width and p is the number of parameters to be fit. If the interferogram has been zero-padded or the spectrum has been apodized then n will be less than the number of data points in the window.

The exact procedure used to derive a profile depends on the atmospheric quantity being measured. In general the procedure is to fit the upward-looking rays first, use the results to scale the overhead profile, and then iterate several times until the results converge. Once the overhead profile is properly scaled, the lower layers are fit in order of descending altitude below the balloon, updating each layer before fitting the next one. The calibration error is estimated as described in Sec. 4.3.2 and added to the fitting error to estimate the total error in fitting each window. Systematic errors such as errors in molecular line parameters are added in quadrature after averaging the results from individual windows.

4.1. MIXING RATIO RETRIEVALS

For each molecule we select a set of spectral windows as follows. For molecules with a large number of transitions in our spectral bands we reject lines which are highly saturated, very weak, have a large excitation energy, or are blended with another line which contributes more than about 10% to the total flux. For molecules with only a few transitions, we relax these constraints and reject only those lines which are blended. We then define a small spectral window around each line, about 0.06 to 0.6 cm^{-1} wide, and fit the vmr , updating the profile as we progress from layer to layer. If a spectral line is too weak in a particular window to give a good fit, then the profile is not updated in order to prevent nonsense values from skewing the rest of the profile. For each ray we vary the vmr in the model layer which has the greatest column density along the line of sight for that ray. For downward rays, this is always the tangent layer. We derive a vmr profile for each window, and compute the final profile by taking the weighted average of the individual profiles. We estimate the error in the final profile by calculating the error in the mean, and inflating this estimate by the square root of the reduced chi-square if it is greater than one. For most layers and molecules, the reduced chi-square is very near one, which implies that we are properly estimating our random errors.

In addition to the optical depth in the spectral lines, each window has a continuum optical depth equal to the sum of the combined contributions of the wings of all lines outside the window. The continuum is dominated by H_2O in the far-infrared and CO_2 and H_2O in the mid-infrared. Stratospheric particles make negligible contributions, since typical particle sizes are much less than a wavelength. Initial values for the continuum opacity are calculated using a parameterized model described by *Clough et al.*, [1989], in which the opacity is a function of H_2O and CO_2 vmr , as well as pressure, temperature, and frequency. We usually make continuum opacity an adjustable parameter, so as to account for nearby line wings which are not included in the initial model.

4.2. TEMPERATURE AND PRESSURE RETRIEVALS

Before retrieving mixing ratios, we correct the initial-guess model atmosphere for errors in the radiosonde data and pointing angle using the $15\mu\text{m}$ band of CO_2 to retrieve atmospheric temperature and pressure. We check the results by using a number of far-infrared O_2 lines ranging from saturated to weak and having excitation energies between 2 and $10kT$. Being able to derive consistent oxygen profiles over a range of pressure and temperature sensitivities gives us confidence that our procedure gives accurate results.

We measure the temperature by calculating synthetic spectra in selected CO_2 -containing windows for each ray, and adjusting the temperature in a single layer while keeping the CO_2 mixing ratio fixed so as to minimize the difference between the actual and calculated spectra. For downward looking rays, we fit the tangent layer, and for overhead rays we fit the overhead layers in order of decreasing altitude above the observer using the rays in order of decreasing elevation angle. The set of spectral windows used to fit each ray depends on the total air mass along the line of sight for that ray. We choose windows which maximize the temperature sensitivity and minimize the sensitivity to the column density for the layer to be fitted. Once all the windows for a given ray have been fitted the results are averaged together to derive the estimated temperature for that layer. We iterate on the overhead rays 4 times, updating the overhead layers after all overhead rays have been fitted. We then proceed to fit the downward looking rays, updating each layer before the next one down is fitted.

The temperature sensitivity function is estimated for each ray by calculating one set of spectra for the spectral range $580\text{--}700\text{ cm}^{-1}$, calculating a second set of spectra after changing the temperature in the layer to be fit by 2%, and then calculating the difference and normalizing the maximum difference value to unity. This procedure is repeated to estimate the column density sensitivity function, this time adjusting the CO_2 mixing ratio. In general, the temperature sensitivity for a

given window increases with increasing optical depth up to a saturation point, and then begins to decrease as the atmosphere becomes opaque. The column density sensitivity function behaves in a similar fashion but saturates at lower optical depth. We subtract the normalized column density sensitivity function from the normalized temperature sensitivity function and select temperature windows from regions where the difference is a maximum. This amounts to choosing windows with optical depth near unity. As the opacity increases from zero, the flux becomes less dependent on the column density while remaining dependent on the temperature at which the gas is radiating. If the optical depth is too high, however, the radiation from the layer to be fitted is absorbed in intervening layers before it reaches the observer. For downward looking rays the geometry is especially favorable for retrievals since about 75% of the total column is within one half scale height of the tangent altitude. The method works less well for layers higher than the layer immediately above the observer. Our set of temperature windows is given in Table 1, as well as the typical column densities for which they are used and the initial elevation angles. The column densities have been calculated for a balloon altitude of 4.8 mb and the initial model atmosphere of our September 1989 balloon flight.

After correcting the model temperatures we retrieve a mixing ratio profile for CO_2 using the set of fourteen windows in the region 572.8 to 620 cm^{-1} listed in Table 2. These windows are chosen as described in Sec. 4.1, and the same windows are used for all rays. We then adjust the pointing angles until the retrieval gives the expected mixing ratio.

The expected CO_2 abundance is estimated by assuming that tropospheric CO_2 is increasing at an annual rate of 1.8 ppm from a reference level of 348 ppm in 1987 [*World Meteorological Organization (WMO)*, 1989]; stratospheric CO_2 is assumed to follow the tropospheric trend, but with a lag of three years and no seasonal variation [*Hall and Prather*, 1993], i.e., $\text{CO}_2 = 348 + 1.8(1987.5 - t)$, where t is the time in years.

To summarize, we adjust the temperature in each layer of our model atmosphere until the

TABLE 1. Temperature windows

| Elevation angle θ | Column (molec cm ⁻²) | Windows (cm ⁻¹) |
|--------------------------|----------------------------------|---|
| 30.0° | 2.06×10^{23} | 615.3-616.6, 619.15-619.36, 684.74-685.12, 686.4-686.6, 689.65-690.1 |
| 0.0° | 3.91×10^{24} | 648.49-649.02, 650.28-650.51, 651.85-652.02, 653.38-653.56, 654.92-655.08, 656.45-656.61, 657.98-658.15, 659.54-659.7, 661.09-661.24, 662.38-662.86, 667.15-668.75, 671.23-671.4, 672.77-672.96, 674.36-674.54, 675.93-676.12, 677.52-677.7, 679.1-679.29, 680.68-680.88, 682.28-682.46, 683.87-684.05, 685.45-685.64, 687.08-687.24, 688.68-688.85, 690.3-690.47 |
| -2.31° | 1.51×10^{25} | 661.22-661.62, 662.8-664.22, 664.7-665.82, 669.82-671.25, 671.4-671.68, 672.5-672.75, 672.95-673.45, 673.95-674.37 |
| -3.03° | 2.93×10^{25} | 649.42-650.24, 650.85-651.7, 652.42-653.2, 654.0-654.7, 655.55-656.25, 657.25-657.73, 658.72-659.25, 660.28-660.8, 661.87-662.32, 675.02-675.62, 676.5-677.23, 678.05-678.8, 679.6-680.05, 681.22-682.1, 682.82-683.7, 684.42-685.3, 686.0-686.95, 687.62-688.52 |
| -3.65° | 5.50×10^{25} | 639.2-639.7, 640.75-641.15, 641.65-642.25, 643.15-643.77, 644.7-645.3, 646.37-646.9, 647.85-648.2, 690.85-691.65, 692.48-693.35, 694.05-695.0, 695.68-696.2 |
| -4.17° | 1.08×10^{26} | 628.48-628.9, 629.5-629.89, 630.55-630.8, 630.98-631.43, 631.55-631.98, 632.5-632.91, 634.0-634.48, 634.68-635.02, 635.78-635.98, 637.15-637.45, 638.85-639.08, 695.75-696.15, 697.3-697.8, 698.95-699.38, 699.5-699.68 |
| -4.62° | 2.14×10^{26} | 620.45-620.8, 620.9-621.1, 622.15-622.32, 622.43-622.63, 623.63-623.83, 624.4-625.0, 625.94-626.45, 627.5-627.88, 628.05-628.33, 629.05-629.32, 629.55-629.85 |

TABLE 2. Pressure windows

| Windows (cm ⁻¹) | | | | |
|-----------------------------|---------------|---------------|-------------|-------------|
| 572.8-573.2 | 574.35-574.85 | 576.0-576.5 | 577.5-578.0 | 582.2-582.7 |
| 583.5-584.5 | 585.5-586.0 | 591.8-592.3 | 593.4-593.9 | 601.2-602.0 |
| 604.4-605.0 | 609.0-609.8 | 612.15-612.95 | 619.0-620.0 | |

normalized flux in saturated regions of the calculated spectrum matches the measured spectrum, and then we adjust the pointing angles to give the expected CO₂ mixing ratio profile. In the next section we discuss potential systematic errors, and after that we provide a cross-check on CO₂

calibration in terms of O_2 .

4.3. ESTIMATION OF UNCERTAINTIES

Our main sources of error are uncertainties in the model atmosphere used to calculate the theoretical spectra and calibration uncertainties in the measured spectra. When estimating the total measurement error we also include line parameter errors and the statistical fitting errors. We test the validity of our error estimates both by checking the chi-square statistic whenever we average together a number of measurements (Sec. 4.1) and by using the oxygen profile as a diagnostic tool (Sec. 4.3.3).

4.3.1. MODEL ATMOSPHERE UNCERTAINTIES

To estimate the effect of errors in the model atmosphere parameters on the retrieved mixing ratio profiles, we find it useful to consider the limiting case of a very strong line, such as the O_2 line at 106.421 cm^{-1} , and a weak line, such as the O_2 line at 187.816 cm^{-1} . As an illustration we will consider the geometry of the -2.31° ray from our September 1989 balloon flight, for which the balloon float pressure is 4.8 mb, the pressure at the tangent height for the -2.31° ray is 8.4 mb, and the temperature in the tangent layer is 235 K.

We define the equivalent width (EW) of a line to be the integral over the spectral window of the difference between spectra calculated with and without the molecule of interest: the EW is therefore the area of the line feature only, since the background is subtracted. Since the spectra are normalized to give dimensionless intensities, the units of EW are wavenumbers (cm^{-1}).

For the -2.31° ray, the EWs of the weak and strong lines are 0.0004 cm^{-1} and 0.02 cm^{-1} , respectively. For both lines the Lorentz line FWHM in the tangent layer is $2\alpha_L = 0.0006\text{ cm}^{-1}$, which is about 0.15 spectral resolution elements unapodized.

In the case of the strong line, adjusting the mixing ratio will have little effect on the flux in the line core where the optical depth is large, and so any change in the EW is due to changes in the

flux in the wings of the line. Since the EW is five resolution elements, the wings are resolved and this means that the spectrum is fitted by matching the flux in the far wings of the line. We can estimate the effect of small errors in atmospheric temperature and pointing angle on the retrieved mixing ratios in this case by assuming constant flux in the line wings. If the continuum opacity is small, the equation giving the temperature dependence of the derived mixing ratio is

$$\frac{\delta(vmr)_T}{vmr} = \left(\frac{5}{2} - \frac{\sigma_u}{3T} - \frac{\Delta z}{H} \right) \frac{\delta T}{T} . \quad (11)$$

where $\sigma_u(\text{cm}^{-1})$ is the transition upper state energy, $\beta = k/hc \simeq 0.695 \text{ cm}^{-1} \text{ K}^{-1}$, T is the model layer temperature, Δz is the vertical layer thickness, and H is the atmospheric scale height. In deriving Eq. (11) we have assumed that the rotational partition function is proportional to T , and that the Lorentz line width is proportional to \sqrt{T} . The dependence on pointing angle, expressed in terms of the pressure in the tangent layer (P), is given by

$$\frac{\delta(vmr)_P}{vmr} = -2.0 \frac{\delta P}{P} . \quad (12)$$

For the O_2 line at 106 cm^{-1} the excitation energy is 544 cm^{-1} , and using a typical value of one half scale height for the layer thickness gives the net result ($\delta T + \delta P$)

$$\text{Saturated } \text{O}_2 \text{ line: } \frac{\delta(vmr)}{vmr} = -1.3 \frac{\delta T}{T} - 2.0 \frac{\delta P}{P} . \quad (13)$$

For the weak line the EW is a fraction of a resolution element, so in this case the fitting routine effectively adjusts the mixing ratio to match the equivalent width without regard to line shape. We have also derived a set of relations similar to Eqs. (11) and (12) by assuming constant equivalent width. In this case, for small continuum opacity, the equation giving the temperature dependence is

$$\frac{\delta(vmr)_T}{vmr} = \left(\frac{5}{2} - \frac{\sigma_u}{\beta T} - \frac{2\Delta z}{H} - \frac{\sigma/\beta T}{1 - e^{-\sigma/\beta T}} \right) \frac{\delta T}{T} , \quad (14)$$

where σ is the frequency at the line center. The expression for the pressure dependence is

$$\frac{\delta(vmr)_P}{vmr} = - \left(\frac{u}{L(u)} \frac{dL(u)}{du} \right) \frac{\delta P}{P} , \quad (15)$$

where $L(u)$ is the Ladenburg and Reiche function [Goody and Yung, 1989], u is given by

$$u = \frac{vmr NS}{2\pi\alpha_L} , \quad (16)$$

N is the total column density in molecules per square centimeter, and S is the line strength in cm. For the O_2 line at 188 cm^{-1} the excitation energy is 1608 cm^{-1} and $u \approx 0.1$. For $u \ll 1$, $L(u) \approx u$, and the net result is

$$\text{Weak } O_2 \text{ line: } \frac{\delta(vm\tau)}{vm\tau} = -10.0 \frac{\delta T}{T} - 1.0 \frac{\delta P}{P} . \quad (17)$$

For these two oxygen lines the pressure dependence varies by a factor of two, while the temperature dependence varies by almost an order of magnitude. This is especially important to consider when attempting to measure abundance ratios, since mixing ratios measured using strong lines will have different systematic errors from those measured from weak lines, and likewise for abundances measured using lines with different excitation energies. This situation can occur when trying to measure isotope ratios where the minor isotope is much less abundant than the major isotope.

As shown in Sec. 4.2, we derive pressures by measuring the CO_2 mixing ratio profile, and as a result the temperature and pressure errors are coupled. The CO_2 lines used in deriving pressure are saturated and have an average excitation energy of 2200 cm^{-1} . Using Eqs. (11) and (12) we derive the following equation relating the uncertainty in pressure to the uncertainties in temperature and CO_2 :

$$\frac{\delta P}{P} = -0.5 \frac{\delta[CO_2]}{[CO_2]} - 5.9 \frac{\delta T}{T} , \quad (18)$$

where $[CO_2]$ is the CO_2 vmr . This relationship gives us the pressure uncertainty in terms of other measureable uncertainties, and can therefore be used to estimate vmr uncertainties for non- CO_2 species in terms of those of CO_2 . Using Eq. (18) to substitute for $\delta P/P$ in Eqs. (13) and (17), and using typical values of 0.5% for $\delta T/T$ and 2.8% for the statistical uncertainty in the measured CO_2 mixing ratio, we estimate vmr errors of 3.6% and 2.5% for O_2 at 106 cm^{-1} and 188 cm^{-1}

respectively, where the uncertainties in temperature and CO₂ mixing ratio have been added in quadrature. These errors are comparable to our statistical fitting errors.

4.3.2. CALIBRATION UNCERTAINTIES

In deriving the final model atmosphere as described above, there is the danger that we are masking errors in normalization, mixing ratio retrievals, or some unexpected systematic error by adjusting the temperature and column density to match the expected CO₂ spectrum. In this section we show that the known systematic calibration errors are small compared to random errors. In the next section we show that the corrected model atmosphere gives sensible results for O₂ retrievals.

The estimated uncertainty in spectral intensity normalization depends on (a) uncertainties in the calibration source emissivity and temperature, and (b) drifts in background emission and instrument response. The blackbody calibration source is a 25 cm diameter, 1.9 cm thick aluminum disk, machined on the front (FIRS-facing) side with a series of concentric V-shaped grooves with 30° vertex angles. The grooved surface is painted with 3M Black Velvet paint, which has a reflectance of less than 4% at normal incidence in our wavelength region [Smith, 1984]. The geometry is such that any ray originating from the primary mirror will experience a minimum of four reflections inside a groove resulting in a net reflectance less than 2.6×10^{-6} , ignoring the angular dependence of the reflectance. There are 3 thermistors mounted on the back of the calibration source at radii of 0, 6.4, and 11.4 cm. We assume that the accuracy of the thermistors is ± 0.6 K, the manufacturing tolerance, which we checked with a single point calibration at 273.15 K. The thermal gradient across the load is estimated from the differences between the three sensors, which is always less than 0.2 K during flight. The thermal gradient between the front and back of the calibrator is assumed to be small, because of the thinness of the paint layer, the large area of contact in the grooves, and the fact that the calibrator is in thermal equilibrium with the surroundings. Therefore, the uncertainty in the calibration source is dominated by the uncertainty in the calibrator temperature.

Drifts in the instrument response are estimated from the measured warm and cold reference spectra by looking at differences between gain and background measurements made at different times. These differences are typically less than 2%, do not grow with the time between measurements, and are inversely correlated with the signal to noise ratio (SNR) in the spectral region being examined. This implies that the changes in gain and background are dominated by the statistical uncertainty in measuring V_w and V_c (see Eq. 4), and that the normalization errors can be reduced by summing normalized spectra. We estimate the effects of these errors on temperature and mixing ratio retrievals by repeating the analysis after changing the estimated gain and background by ± 1 standard deviation. Roughly, an error of 2% in the normalization corresponds to an error in atmospheric temperature of 3.4 K at 100 cm^{-1} and drops to 1.1 K at 650 cm^{-1} for a nominal temperature of 235 K. The maximum uncertainty in the atmospheric temperature due to calibration errors is the quadrature sum of the normalization and thermistor calibration errors, or 1.2 K for the frequency range covered by the windows listed in Table 1. The minimum uncertainty in atmospheric temperature which may be obtained by averaging many measurements together is equal to the thermistor calibration error, 0.6 K. A comparison of our retrieved temperatures (including normalization errors) with radiosonde measurements for the March 23, 1993 balloon flight is shown in Fig. 2. Performing the ray tracing calculation described in Sec. 3.1 through a model atmosphere with the temperature profile shown here will result in effective temperatures $T_{\text{eff}}(i)$ that match our measured temperatures. In Fig. 3 we show the initial and final CO_2 *vmr* profiles for the March 23 flight, i.e., before and after correcting the temperatures and pointing angles.

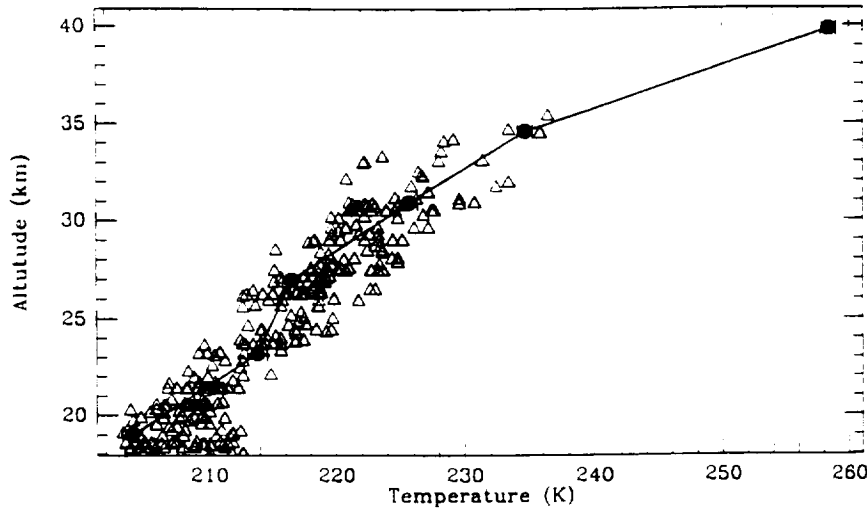


Fig. 2. Temperature retrieval for the March 23, 1993 balloon flight. Spectroscopically measured temperatures are indicated by the filled circles, and radiosonde data by the open triangles. Spectroscopic errors include the uncertainty in calibration and statistical errors.

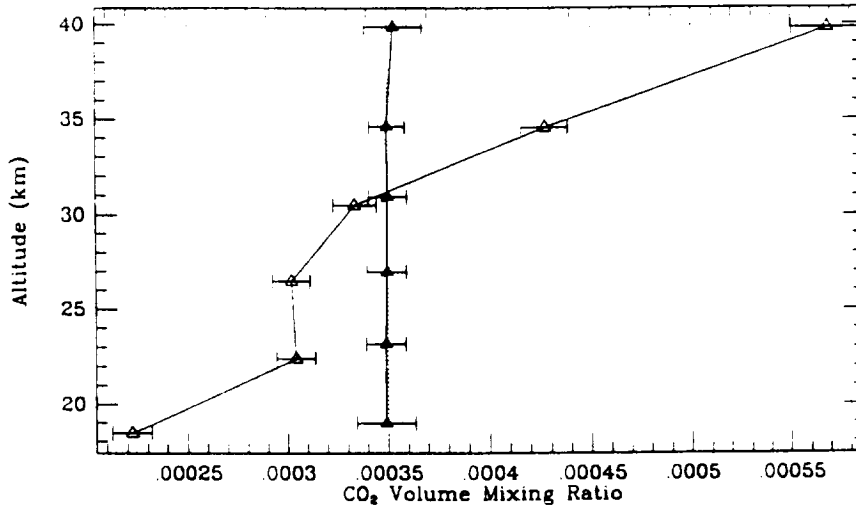


Fig. 3. CO₂ mixing ratio profile for the March 23, 1993 balloon flight. Open and filled symbols indicate profiles derived from the initial and final model atmospheres, respectively. The initial model atmosphere is based on temperatures from radiosonde measurements and pressures derived from the commanded viewing angles of the light-collecting telescope on board the flight gondola. The final model atmosphere is based on temperatures and pressures derived from the 16 μm band of CO₂, as described in the text. Error bars include calibration and statistical uncertainties only. The CO₂ mixing ratio was assumed to be 350 ppm for this example.

4.3.3. O₂ PROFILE

As a test of overall calibration procedure, we present in Fig. 4 a number of O₂ profiles for the same spectra as Figs. 2 and 3, derived from three different sets of lines. The first set consists of three strong lines, having $\text{EW}/\alpha_L (= 2\pi L(u))$ greater than 50 and an average excitation energy of

440 cm⁻¹. The second set consists of nine weak lines having EW/α_L less than 5.5 and an average excitation energy of 1530 cm⁻¹. The third set consists of four weak lines of ¹⁸O¹⁶O having EW/α_L less than 2.0 and an average excitation energy of 500 cm⁻¹. Any errors in temperature or pressure should have quite different effects on these three line subsets as can be seen by evaluating Eqs. (11) through (17). The final profiles in Fig. 4 are in much better agreement with the expected O₂ abundances than are the initial profiles. However we note that the strong O₂ lines tend to be biased toward a high *vmr*, and weak O₂ lines tend to be biased low, both at about the one-sigma level. This suggests that the different O₂ line sets have internal line-parameter biases on the order of about 10%. In particular, we anticipate that the principal line-parameter uncertainties are in the air-broadening coefficients of the strong lines, possibly as much as 23%, as discussed in *Chance et al.* [1991b]. On the other hand, the weak isotopomer lines appear to give an unbiased O₂ *vmr* profile, possibly because these lines are unaffected by either pressure-broadening uncertainties or high-J line strength uncertainties.

In a previous paper [Abbas and Traub, 1992] we explicitly compared two methods of analyzing FIRS-1 spectra; one based on empirical viewing angles derived from the same 3 strong lines of O₂ used in the present work. In the Abbas and Traub paper we found that the O₂-derived angles gave *vmr* profiles of O₃, H₂O, HF, and HCl which were usually, but not always, closer to the mean values as determined from other experiments which flew simultaneously. By comparison, the present paper shows that if O₂ lines are used for viewing angle calibration, then it is important to employ both weak and strong lines, as well as isotopomer lines, to reduce potential bias in the derived *vmr*.

The temperature, pressure, and oxygen fitting results are summarized in Table 3. The uncertainty in the least significant digit is indicated in parentheses for all measured quantities. For each ray, the effective altitude, pressure, and temperature are the air-mass-weighted quantities along the line of sight in the layer which was fitted, as described in Sec. 3.1. The errors in temperature and

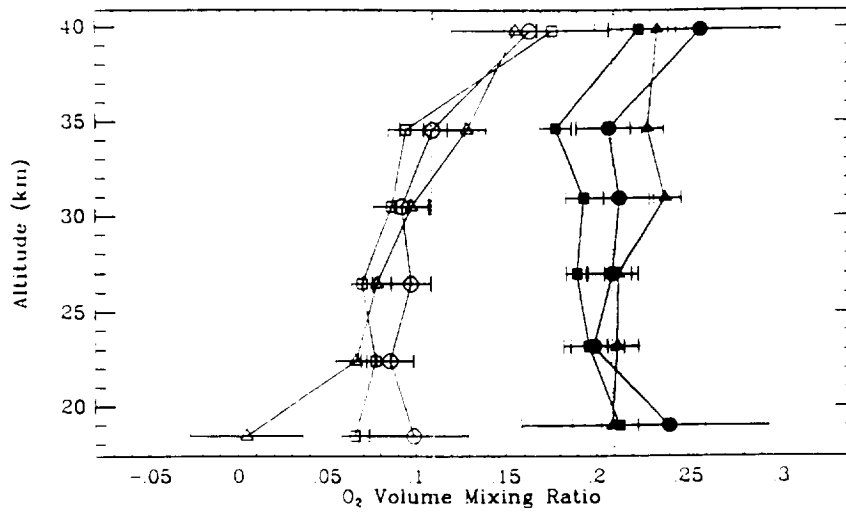


Fig. 4. O_2 mixing ratio profile for the March 23, 1993 balloon flight. Open and filled symbols indicate profiles derived from the initial and final atmosphere models respectively (cf. Fig. 3 caption). Triangles indicate the saturated line set, squares indicate the weak line set, and circles indicate the weak isotopomer set. Error bars include calibration and statistical uncertainties only. For clarity, the initial profiles are shifted by -0.1 in vmr

mixing ratio include calibration and statistical uncertainties. The errors in the final angle, altitude, and pressure are determined by the uncertainty in the CO_2 mixing ratio profile. As described earlier, the errors in temperature, pressure, and CO_2 mixing ratio are all coupled. The oxygen profile is an average of all 16 strong, weak, and isotopomer-line profiles.

TABLE 3. Initial and final models: March 1993

| Layer fit | Initial | | | | Final | | | | | |
|--------------|--------------------------|-------------------|-------------------|------------------|--------------------------|-------------------|-------------------|------------------|-------------------|-----------|
| | θ ($^\circ$) | Z_{eff} (km) | P_{eff} (mb) | T_{eff} (K) | θ ($^\circ$) | Z_{eff} (km) | P_{eff} (mb) | T_{eff} (K) | $[CO_2]$ (ppm) | $[O_2]$ |
| 1 | 30.0 | 48.0 | 0.830 | 254.5 | 29.2(16) | 47.80(0.1) | 0.849(0.1) | 249.1(49) | 261(54) | 0.249(20) |
| 2 | 0.00 | 39.8 | 2.79 | 243.3 | 0.06(6) | 39.80(4) | 2.78(2) | 256.8(1) | 353(14) | 0.221(4) |
| 3 | -2.32 | 34.5 | 5.89 | 231.2 | -2.31(1) | 34.60(7) | 5.78(5) | 235.8(3) | 350(10) | 0.208(4) |
| 4 | -3.04 | 30.5 | 10.8 | 223.6 | -2.95(2) | 30.90(9) | 10.0(1) | 226.4(4) | 350(10) | 0.210(4) |
| 5 | -3.66 | 26.4 | 20.0 | 217.2 | -3.59(1) | 27.00(9) | 18.3(3) | 217.5(3) | 350(10) | 0.199(3) |
| 6 | -4.18 | 22.4 | 38.0 | 211.6 | -4.08(1) | 23.20(8) | 33.4(4) | 213.5(5) | 349(10) | 0.202(4) |
| 7 | -4.63 | 18.4 | 72.3 | 208.8 | -4.58(1) | 19.00(12) | 66.5(12) | 205.2(5) | 349(14) | 0.218(8) |

5. RETRIEVALS FROM DC-8 SPECTRA

The DC-8 cruises at a pressure altitude of about 11 ± 1 km, which is usually, but not always, above both the tropopause and the hydropause. We limit our viewing angles to positive elevations, because the bulk of the stratosphere is overhead, and, also, negative angles are heavily obscured by tropospheric water vapor absorption. As mentioned earlier, we divide the atmosphere above the aircraft into nine layers, with the bottom of the lowest layer set equal to the aircraft altitude at the time of the measurement. We choose the other layer boundaries to divide the overhead column evenly, with the exception of creating somewhat thinner layers near the aircraft altitude in order to avoid excessive smearing of the temperature profile near the tropopause. In each 700-sec observing sequence we record spectra at elevation angles of 0° , 1° , 2° , 4° , 8° , 16° , and 32° . The geometry is such that observations made at small elevation angles are most sensitive to the lower layers, while observations made at larger angles are increasingly sensitive to the upper layers.

We use two independent algorithms to retrieve overhead column densities from our spectra: (a) the singular-value decomposition (SVD) method, and (b) the non-linear least-squares (NLLS) method. The advantages of the SVD method are that vertical profile information can be recovered, in addition to column densities, and that it is also a very fast technique because it is linear in the variables. The advantage of the NLLS method is that it is potentially more accurate, because there are no interpolation or linear extrapolation approximations; however at present it is limited to the recovery of column densities. In practice, we find that both methods give column densities which agree very closely. The algorithms are sketched in sections 5.1 and 5.2, followed in 5.3 by a short discussion of calibration uncertainties in the aircraft spectra.

5.1. SINGULAR-VALUE DECOMPOSITION METHOD

In the SVD method [Press *et al.*, 1986] we set up a single matrix equation expressing the observable quantities as linear functions of model parameters, and we solve the matrix equation. We linearize the physical problem by defining the inputs and outputs as perturbations of an assumed nominal state; this is a valid procedure whenever the final state can be expressed as the sum of an initial state and a linear power series expansion about that state.

In the present application, the model parameters are scaling factors applied to the initial-guess mixing ratio profiles: for example, if only one parameter is used, the entire vertical column is scaled, or if four parameters are used, then the mixing ratio profile in four independent vertical regions can be adjusted separately. The maximum number of independent parameters which can be used depends upon, first, the extent to which the observable quantities are decoupled, and second, the SNR. In our case, the curvature of the earth and the optical depth of the spectral lines act as decoupling agents, so that the upward-looking rays preferentially sample the distant, upper stratosphere, and the more horizontal-looking rays tend to sample the closer, lower stratosphere. Our pre-flight numerical simulations, with an assumed SNR, showed that we could extract four independent vertical scaling factors. In practice, the in-flight SNR was lower than anticipated, so we reduced the number of parameters to one.

Specifically, we measure the equivalent width (EW) for a particular spectral line and elevation angle, and compare it to the EW calculated for the initial mixing ratio. We repeat the measurement for N elevation angles and L lines, resulting in a total of $J = NL$ measurements for each molecule. We express small differences between the measured and calculated EW in terms of small changes in the mixing ratio in each layer of the model atmosphere. We divide the atmosphere into M layers, where $vmr_i(0)$ is the initial mixing ratio for layer i , and $EW_j(0)$ is the calculated equivalent width

for measurement j . Then, in the linearized situation, we have

$$EW_j - EW_j(0) = \sum_{i=1}^M \frac{d(EW_j)}{d(vmr_i)} (vmr_i - vmr_i(0)) , \quad (19)$$

where j runs from 1 to J . We define the dimensionless quantities

$$b_j = \frac{EW_j - EW_j(0)}{\sigma_j} , \quad (20)$$

$$a_i = \frac{vmr_i - vmr_i(0)}{vmr_i(0)} , \quad (21)$$

where σ_j is the statistical error in measuring EW_j . Then Eq. (19) takes the form

$$\mathbf{b} = \mathbf{A} \cdot \mathbf{a} , \quad (22)$$

where \mathbf{b} is a $J \times 1$ matrix with elements b_j , \mathbf{a} is an $M \times 1$ matrix with elements a_i , and the sensitivity matrix \mathbf{A} is a $J \times M$ matrix with dimensionless elements

$$A_{ji} = \frac{vmr_i(0)}{\sigma_j} \frac{d(EW_j)}{d(vmr_i)} . \quad (23)$$

We solve Eq. (22) using the method of SVD. If $J > M$, then \mathbf{A} can be written as the product of three matrices, $\mathbf{A} = \mathbf{U} \cdot \mathbf{W} \cdot \mathbf{V}^T$, where \mathbf{U} is a $J \times M$ column-orthogonal matrix ($\mathbf{U}^T \cdot \mathbf{U} = \mathbf{I}$), \mathbf{W} is an M by M diagonal matrix whose elements are greater than or equal to zero, and \mathbf{V}^T is the transpose of an orthogonal $M \times M$ matrix. Solving Eq. (22) for \mathbf{a} gives the result

$$\mathbf{a} = \mathbf{V} \cdot \mathbf{W}^{-1} \cdot \mathbf{U}^T \cdot \mathbf{b} , \quad (24)$$

where \mathbf{W}^{-1} is the $M \times M$ diagonal matrix whose elements are given by $1/W_{ii}$ when W_{ii} is significantly greater than the computer roundoff error, and zero otherwise. The SVD solution is equivalent to the best fit solution in a least squares sense. The variance $\sigma^2(a_j)$ of the estimate a_j is given by

$$\sigma^2(a_j) = \sum_{i=1}^M \left(\frac{V_{ji}}{W_{ii}} \right)^2 . \quad (25)$$

To apply the SVD method to our DC-8 spectra, we numerically calculate the EW derivatives in Eq. (23) for a number of different observation angles, aircraft altitudes, continuum opacities, and column densities, and then interpolate to find the sensitivity matrix for each set of observations. The derivatives can be calculated ahead of time, thus reducing the time required for data processing. The initial mixing ratio profiles are from the ATMOS-based set mentioned in the balloon section above, and the initial temperature profile is representative of high-latitude winter conditions. By scaling these profiles to a variety of different total column densities, and interpolating between the corresponding sensitivity matrices, we insure that linearity is maintained.

Our initial data analysis with the four-parameter model atmosphere showed that the SNR was insufficient to reliably extract this many parameters. Therefore we opted for the highly-stable one-parameter algorithm which gives total column abundances. All FIRS-2 aircraft flight data were reduced with this method, and the results were published in the AASE-II preliminary CD-ROM data set [Gaines *et al.*, 1992].

In general the SVD algorithm is fast and accurate, but, in the version described above, two desirable features are lacking: the ability to utilize actual (measured) temperature profiles, and the ability to use FIRS-2 observations to determine vertical displacements of the stratosphere. In fact, both capabilities could be built into the SVD method. For example, a grid of temperature profiles could be set up, and a set of sensitivity matrices calculated for each; the measured temperature profile could then be matched to the nearest member of this set, and an interpolated matrix found, as with the other three interpolations above. Similarly, vertical displacements could be modeled, sensitivity matrices calculated for a grid of displacement values, and another interpolation performed. This would increase the dimensionality of the interpolations, from three to five.

However, rather than following the path of adding complexity to the basically simple SVD method, we decided instead to switch to the NLLS method, which offered all the required flexibility in return for an acceptable increase in computing time. This method is described next.

5.2. NON-LINEAR LEAST-SQUARES METHOD

The NNLS method for aircraft spectra is a modified version of the corresponding program for balloon spectra. The overhead atmosphere is divided into 9 spherical shell layers. Pressure and temperature profiles are taken from the “curtain file” of meteorological data along the aircraft flight track at the time of observation, provided by the National Meteorological Center via Goddard Space Flight Center (see, for example, *Newman, et al.* [1993]). Effective temperatures and pressures are determined for each layer, and initial mixing ratios are assigned from the standard mid-latitude set of profiles.

As the winter polar stratosphere cools, it becomes denser, which sets up a large-scale horizontal vortex and a vertical subsidence. The secular subsidence effectively drops all mixing ratio profiles towards lower altitudes. To analyze our observations in the polar vortex during AASE-II, we separate the effects of subsidence and chemical change as follows: (a) use HF as a tracer molecule to determine the subsidence, using a NLLS method; (b) apply this subsidence to the profiles of all other species; (c) adjust the magnitude of the vmr profiles to match the observed spectra, again using a NLLS method.

We follow *Toon et al.* [1992] in defining the subsidence factor s as the sole parameter in a linear transformation of the altitude from z to z' , where

$$\begin{aligned} z' &= (1 + s)z , \\ vmr'(z) &= vmr(z') . \end{aligned} \tag{26}$$

Here $vmr(z)$ is the mid-latitude mixing ratio profile, and $vmr'(z)$ is the subsided profile. We use HF as a tracer because it is chemically inactive in the stratosphere [*Brasseur and Solomon*, 1984], so that changes in the overhead column reflect purely vertical motions in the stratosphere, not chemistry. We measure the subsidence by finding the value of s which minimizes the difference, in the sense of least squares, between the measured spectrum and the spectrum calculated using the

subsided mixing ratio profile for the HF line at 163.9362 cm^{-1} . We determine a single value for the subsidence for each 700-sec set of observation angles, using a weighted average value from the 4° to 32° rays, where the weights are determined from the residuals, the correlation matrix of adjustable parameters, and number of degrees of freedom in the NLLS fitting procedure.

New initial *vmr* profiles are calculated for each species using the subsidence parameter for the observation set and Eq. 26. Water vapor is treated separately: the initial stratospheric profile is computed using the subsidence formula for altitudes above the hydropause, and below this point the tropospheric component is added independently. The hydropause is defined here as the lowest altitude at which the lapse rate equals 2 K/km, about 0.2 times the tropospheric value. We found this step to be useful because the DC-8 occasionally flew below the hydropause, causing the water column to increase dramatically. For all species the optimum scaling factor for the corresponding *vmr* profile is then calculated by the NLLS method, and a weighted average value formed. For water, the scaling is applied to the stratospheric component only.

All FIRS-2 aircraft flight data were reduced with the NLLS method, and the results were published in the AASE-II final CD-ROM data set [Gaines *et al.*, 1993]. Although we have not made a formal comparison of the results of the two data analysis methods, visual inspection of the derived column abundances suggests that the NLLS method performed marginally better. We believe that this is due to the fact that the NLLS method more closely simulates the atmospheric conditions, through the use of (a) actual *vs.* nominal temperature profiles, (b) subsided *vs.* non-subsided *vmr* profiles, (c) scaling the full *vmr* profile *vs.* scaling only a selected segment, and (d) for water, separating the tropospheric and stratospheric contributions.

5.3. CALIBRATION UNCERTAINTIES

The SNRs of individual spectra on the DC-8 were lower than on a balloon platform, because of the relatively higher scan rate, and the much higher vibration level. As stated earlier, the temperature difference between the two blackbody calibration sources on the DC-8 was only 45 to 60 K. The lower SNR together with the small calibration temperature difference results in a typical uncertainty in determining the spectral baseline of about 5% of the normalized scale. The uncertainty in the gain is approximately equal to the gain error for the balloon spectra (roughly 0.5%). The coupling of these normalization errors and the high level of the continuum has a profound effect on the retrievals. Since the baseline correlates highly with the continuum, this calibration error strongly affects the calculated opacity of the continuum of the spectrum, which in turn affects the calculated equivalent width for saturated transitions. We estimate the effect of the normalization error on the measured ratio $EW/EW(0)$ to be

$$\delta \left(\frac{EW}{EW(0)} \right) = \left(\delta g - \delta b \frac{B(\sigma, T)}{B(\sigma, T_{ref})} \right) e^{\tau_c} , \quad (27)$$

where δg is the gain error, δb is the baseline error, and τ_c is the optical depth of the continuum. Because of the e^{τ_c} term, errors are relatively high when the aircraft altitude is below either the tropopause or cirrus clouds, where high H_2O gives high τ_c .

6. SUMMARY

The FIRS-2 far-infrared spectrometer has successfully flown on 8 balloon flights from 1987 through 1993, obtaining about 2160 spectra during 108 hours of operation at an average altitude of 38 km, resulting in measurements of volume mixing ratio (*vmr*) profiles of 15 species and 6 isotopomers, with a minimum uncertainty of about 3% in each 4 km vertical layer, derived from the analysis of over 288 spectral windows.

The FIRS-2 has also successfully flown on 13 DC-8 aircraft flights in 1992, obtaining over 12900 spectra during 140 hours of operation at an average altitude of 11 km, resulting in measurements of column abundances of 6 species and 2 isotopomers, with a median column uncertainty of about 10%, from the analysis of 41 spectral windows.

In this paper, we discuss selected instrumental attributes, and focus on the topics of data reduction, estimation of random and systematic errors, retrieval of mixing ratio profiles, and the estimation of temperature and pressure profiles.

REFERENCES

- Abbas, M. M., and Traub, W. A., Stratospheric minor constituent distributions from far-infrared thermal emission spectra, *J. Geophys. Res.*, *97*, 18,035-18,045, 1992.
- Bell, R. J., *Introductory Fourier Transform Spectroscopy*, Academic Press, New York, 141-152, 1972.
- Brasseur, G., and Solomon, S., *Aeronomy of the middle atmosphere*, Reidel, Dordrecht, Holland, 1984.
- Carlotti, M., Di Lonardo, G., Fusina, L., Trombetti, A., and Carli, B., The far-infrared spectrum of hypochlorous acid, HOCl, *J. Molec. Spectrosc.*, *141*, 29-42, 1990.
- Chance, K. V., Jennings, D. A., Evenson, K. M., Vanek, M. D., Nolt, I. G., Radostitz, J. V., and Park, K., Pressure broadening of the 118.455 cm^{-1} rotational lines of OH by H₂, He, N₂, and O₂, *J. Molec. Spectrosc.*, *146*, 375-380, 1991a.
- Chance, K. V., Traub, W. A., Jucks, K. W., and Johnson, D. G., On the use of O₂ spin-rotation lines for elevation angle calibration of atmospheric thermal emission spectra, *Int. J. Infrared Millimeter Waves*, *12*, 581-588, 1991b.
- Chance, K. V., Jucks, K. W., Johnson, D. G., and Traub, W. A., The Smithsonian Astrophysical Observatory database SAO92, submitted to *J. Quant. Spectrosc. Radiat. Transfer*.
- Ciarpallini, P., Measure of the absorption coefficient of MylarTM, *STC Tech. Rep. 2628*, Science and Technology Corp., Hampton, VA, 1992.
- Clough, S. A., Kneizys, F. X., and Davies, R. W., Line shape and the water vapor continuum, *Atmospheric Research*, *23*, 229-241, 1989.
- Cohen, E. A., and Pickett, H. M., The dipole moment of hydrogen peroxide, *J. Mol. Spectros.*, *87*, 582-583, 1981.
- Coyle, L. M., Aurilio, G., Nystrom, G. U., Bortz, J., Nagy, B. G., Chance, K. V., and Traub,

- W. A., Design of a single-axis platform for balloon-borne remote sensing, *Rev. Sci. Instr.*, **57**, 2512-2518, 1986.
- Dabbousi, O. B., Meerts, W. L., De Leeuw, F. H., and Dymanus, A., Stark-Zeeman hyperfine structure of H^{79}Br and H^{81}Br by molecular-beam electric-resonance spectroscopy, *Chem. Phys.*, **2**, 473-477, 1973.
- Di Lonardo, G., Fusina, L., De Natale, P., Inguscio, M., and Prevedelli, M., The pure rotation spectrum of HBr in the submillimeter-wave region, *J. Molec. Spectrosc.*, **148**, 86-92, 1991.
- Gaines, S., Hathaway, P., and Hipskind, S., Eds., Airborne Arctic Stratospheric Expedition II. Preliminary Mission Dataset, NASA/UARP-004 Edition 1, NASA Ames Research Center, July 1992.
- Gaines, S., Hathaway, P., and Hipskind, S., Eds., Airborne Arctic Stratospheric Expedition II. Mission Dataset, NASA/UARP-004 Edition 2, NASA Ames Research Center, July 1993.
- Goody, R. A., and Yung, Y. L., *Atmospheric radiation, theoretical basis*, Oxford University Press, New York, NY, 1989.
- Hall, T. M., and Prather, M. J., Simulations of the trend and annual cycle in stratospheric CO_2 , *J. Geophys. Res.*, **98**, 10,573-10,581, 1993.
- Kaiser, E. W., Dipole moment and hyperfine parameters of H^{35}Cl and D^{35}Cl , *J. Chem. Phys.*, **53**, 1686-1703, 1970.
- Masset, F., Lechuga-Fossat, L., Flaud, J.-M., Camy-Peyret, C., Johns, J. W. C., Carli, B., Carlotti, M., Fusina, L., and Trombetti, A., The far infrared spectrum of H_2O_2 observed and calculated rotational levels of the torsional states: $(n, \tau) = (0, 1), (0, 3)$ and $(1, 1)$, *J. Phys. France*, **49**, 1901-1910, 1988.
- Muenter, J. S., and Klemperer, W., Hyperfine structure constants of HF and DF, *J. Chem. Phys.*, **52**, 6033-6037, 1970.
- Newman, P., Lait, L. R., Schoerberl, M., Nash, E. R., Kelly, K., Fahey, D. W., Nagatani, R.,

- Toohey, D., Avallone, L., Anderson, J., Stratospheric meteorological conditions in the Arctic polar vortex, 1991 to 1992, *Science*, *261*, 1143-1146, 1993.
- Nolt, I. G., Radostitz, J. V., Di Lonardo, G., Evenson, K. M., Jennings, D. A., Leopold, K. R., Vanek, M. D., Zink, L. R., Hinz, A., and Chance, K. V., Accurate rotational constants of CO, HCl and HF: spectral standards for the 0.3 to 6 THz (10 to 200 cm^{-1}) region, *J. Molec. Spectrosc.*, *125*, 274-287, 1987.
- Pine, A. S., and Looney, J. P., N_2 and air broadening in the fundamental bands of HF and HCl, *J. Molec. Spectrosc.*, *122*, 41-55, 1987.
- Poynter, R. L., and Pickett, H. M., Submillimeter, millimeter, and microwave spectral line catalogue, *JPL Pub. 80-23, Rev. 2*, Jet Propulsion Laboratory, Pasadena, CA, 1984.
- Press, W. H., Flannery, B. P., Teukolsky, S. A., and Vetterling, W. T., *Numerical recipes: the art of scientific computing*, Cambridge University Press, New York, NY, 1986.
- Revercomb, H. E., Buijs, H., Howell, H. B., LaPorte, D. D., Smith, W. L., and Sromovsky, L. A., Radiometric calibration of IR Fourier transform spectrometers: solution to a problem with the High-Resolution Interferometer Sounder, *Appl. Opt.*, *27*, 3210-3218, 1988.
- Rothman, L. S., Gamache, R. R., Tipping, R. H., Rinsland, C. P., Smith, M. A. H., Benner, D. C., Devi, V. M., Flaud, J.-M., Camy-Peyret, C., Perrin, A., Goldman, A., Massie, S. T., Brown, L. R., and Toth, R. A., The HITRAN molecular database: editions of 1991 and 1992, *J. Quant. Spectrosc. Radiat. Transfer*, *48*, 469-507, 1992.
- Smith, S. M., Specular reflectance of optical-black coatings in the far infrared, *Appl. Opt.*, *23*, 2311-2326, 1984.
- Toon, G. C., Farmer, C. B., Schaper, P. W., Lowes, L. L., Norton, R. H., Schoeberl, M. R., Lait, L. R., and Newman, P. A., Evidence for subsidence in the 1989 arctic winter stratosphere from airborne infrared composition measurements, *J. Geophys. Res.*, *97*, 7963-7970, 1992.
- Traub, W. A., and Stier, M. T., Theoretical atmospheric transmission in the mid- and far-infrared

- at four altitudes. *Appl. Opt.*, 15, 364-377, 1976.
- Traub, W. A., Chance, K. V., Brasunas, J. C., Vrtilek, J. M., and Carleton, N. P., Use of a Fourier transform spectrometer on a balloon-borne telescope and at the Multiple Mirror Telescope (MMT), *SPIE* 331, 208-218, 1982.
- Traub, W. A., Chance, K. V., and Coyle, L. M., Performance of a single-axis platform for balloon-borne remote sensing, *Rev. Sci. Instr.*, 57, 2519-2522, 1986.
- Traub, W. A., Chance, K. V., Johnson, D. G., and Jucks, K. W., Stratospheric spectroscopy with the far-infrared spectrometer (FIRS-2): overview and recent results, *SPIE* 1491, 298-307, 1991.
- Varberg, T. D., and Evenson, K. M., Accurate far-infrared rotational frequencies of carbon monoxide, *Ap. J.*, 385, 763-765, 1992.
- Watson, D. M., Genzel, R., Townes, C. H., Werner, M. W., and Storey, J. W. V., Detection of far-infrared [O_I] and [O_{III}] emission from the galaxy M82, *Ap. J. Lett.*, 279, L1-L4, 1984.
- World Meteorological Organization, Global Ozone Research and Monitoring Project, Scientific assessment of stratospheric ozone: 1989, pp. 245-246, *Rep. No. 20*, Geneva, Switzerland, 1989.

APPENDIX C

The Smithsonian Astrophysical Observatory database SAO92

PRECEDING PAGE BLANK NOT FILMED

The Smithsonian Astrophysical Observatory Database SAO92

K. Chance, K. W. Jucks, D. G. Johnson, and W. A. Traub
Harvard-Smithsonian Center for Astrophysics, Cambridge, MA, USA

ABSTRACT

The Smithsonian Astrophysical Observatory (SAO) maintains a molecular line database (the SAO line database) for the analysis of atmospheric spectra in the far infrared and longer-wave mid infrared, from 10-800 cm^{-1} . This database combines the best currently available line parameters, including the HITRAN^{1,2} molecular database, the JPL submillimeter, millimeter, and microwave spectral line catalog³ (JPLSMM), and other available measurements and calculations. The current version of the database contains 154,895 lines from H_2O , CO_2 , O_3 , N_2O , CO , CH_4 , O_2 (including the $^1\Delta$ state), NO , SO_2 , NO_2 , NH_3 , HNO_3 , OH , HF , HCl , HBr , HI , ClO , OCS , H_2CO , HOCl , HCN , H_2O_2 , $\text{O}(^3\text{P})$, and HO_2 . The database is available in both HITRAN-type 80 character (SAO92) and 100 character (SAO92A) formats.

INTRODUCTION

Far infrared techniques have now been successfully used in thermal emission from balloon-borne stratospheric spectrometers to measure atmospheric OH , HO_2 , H_2O_2 , H_2O (including a number of hot bands and minor isotopic species), $\text{O}(^3\text{P})$ atoms (in the mesosphere and thermosphere), O_2 , O_3 (including a number of hot bands and minor isotopic species), HCl , HOCl , HF , NO_2 , HCN , HNO_3 , and a significant upper limit for HBr . The SAO FIRS-2 balloon-borne spectrometer, which is configured to take spectra in the far infrared from 80-210 cm^{-1} , has made measurements of most of these species. FIRS-2 also has a measurement channel in the longer-wave mid infrared from 350-700 cm^{-1} , where CO_2 , HNO_3 , N_2O , and H_2O have been measured. The analysis of flight spectra obtained with this instrument is the prime motivation for maintaining the SAO database. Our concern has been to perform the best possible quantitative analyses of the flight spectra to obtain atmospheric measurements, including a rigorous consideration of the effects of line parameters and their uncertainties on the analysis. This consideration has led in some cases to laboratory measurements and calculations specifically aimed at the improvement of line parameters in order to support the analysis of flight spectra.⁴⁻¹⁰

Figure 1 shows a summary of the result of fitting of FIRS-2 flight spectra (in this case from a balloon flight from Fort Sumner, NM in the fall of 1989) used to obtain atmospheric concentration profiles. This figure provides a visual summary of most of the current thermal infrared stratospheric measurement capability; it is these molecules whose measurement must be supported by an appropriate database. A typical portion of a summed limb-scan of FIRS-2 spectra from the fall 1989 flight, which illustrates the level of detail available in this type of measurement is shown in Figure 2. This portion of the summed (50 min. integration per spectrum) limb-scan, from 99-100 cm^{-1} , includes emission lines from the entire dynamic range of far infrared measurement capability, from the very strong H_2O lines near 99.1 cm^{-1} , to the very weak lines visible at below the 1% level of the spectra (the signal to noise ratio in these spectra is >500). Figure 3 shows the result of an analysis of FIRS-2 spectra to determine the largest measurable far infrared features of those species we measure in our spectra (this includes one upper limit, HBr). This analysis represents the average midday observing conditions of Figs. 1 and 2, for an atmospheric tangent

height of 32 km. This altitude is chosen because it is representative of mid-stratospheric conditions and it is the best altitude for FIRS-2 measurements to support this type of analysis. For convenience in discussing far infrared atmospheric measurements, the approximate limits where lines are fully saturated and fully unsaturated are noted on the figure. The current detection limit for the FIRS-2 instrument (appropriate for several hours of integration time, i.e., the most that can reasonably be obtained at one observation angle during a balloon flight) is also noted.

Our experience in analyzing flight spectra in the FIRS-2 spectral range has been that the traditional databases, HITRAN and JPLSMM, have often proved inadequate for accurate analysis and that, in any case, it has been necessary to review the original literature in order to assess uncertainties. The SAO database is the natural outcome of this process. It is the result of an ongoing review of published data and the inclusion of more recent laboratory measurements and calculations. As such, the working database is in a continual state of change. The version described here is current as of November, 1993. The SAO database does not include uncertainties in the molecular parameters except for those that are included in transitions taken from HITRAN. In the analysis of FIRS-2 flight spectra, our standard practice is to use molecular parameter uncertainties taken from the original literature whenever possible. Thus we do not find it necessary to explicitly include them on the database at this time.

The molecule numbering follows the HITRAN convention for molecules 1-28, with additional molecules defined as 29-36. Number 35 is used as a dummy molecule, for instances where unidentified lines must be added on a temporary basis during the investigation and fitting of spectra. Unless otherwise noted, isotope ratios have been adopted from HITRAN. In several cases (notably H_2O and O_3) minor isotopic and hot band lines have been assigned separate molecule numbers for convenience in spectrum fitting. As in HITRAN (but not JPLSMM), isotopic abundances are included in the catalogued intensities. Changes in line positions necessitated by observations and fitting of atmospheric spectra are noted in the discussion below. The position changes included to date are by no means exhaustive, but are what have been discovered during the fitting of atmospheric spectra from the SAO FIRS-2 FTS instrument.

We maintain both random-access and sequential-access versions of the 80-character and 100-character databases, as well as files for the individual molecules. The sequential access versions are what are normally distributed to interested users. The sequential access files are SAO92n.DAT and SAO92An.DAT, $n = 1-8$. The lines are in 100 cm^{-1} bins, where $100 \times n$ is the upper limit, in cm^{-1} , for each file.

DATABASE FORMATS

80 Character Database. Line positions are now all in the F10.6 format, to keep increased accuracy above 100 cm^{-1} . The format is an "old AFGL" one (see Ref. 1 for details on quantum numbers):

| | | | | | | | | |
|-------|---------|------|-------|-----|-----|----|----|----|
| F10.6 | 1PE10.3 | F5.3 | F10.3 | 2A8 | 2A9 | 4X | I4 | I3 |
| a | b | c | d | e | f | | g | h |

a. Position (cm^{-1})

b. Intensity (cm, at 296 K)

c. Air pressure-broadening coefficient (HWHM, $\text{cm}^{-1}\text{ atm}^{-1}$)

- d. Lower state energy (cm^{-1})
- e. Vibrational quantum numbers
- f. Rotational, electronic, and hyperfine quantum numbers
- g. HITRAN isotope code
- h. Molecule number

Note that portions of e-g are missing for some non-HITRAN transitions.

100 Character Database. This is in the current HITRAN format (see Refs. 1 and 2 for details on quantum numbers and indices):

```
I2 I1 F12.6 E10.3 E10.3 F5.4 F5.4 F10.4 F4.2 F8.5 I3 I3 A9 A9 3I1 3I2
a  b  c      d      e      f      g      h      i      j      k  l  m  n  o  p
```

- a. Molecule number
- b. Isotope number (1 = most abundant, etc.)
- c. Position (cm^{-1})
- d. Intensity (cm. at 296 K)
- e. Transition probability (Debye^2)
- f. Air pressure-broadening coefficient (HWHM, $\text{cm}^{-1} \text{atm}^{-1}$)
- g. Self pressure-broadening coefficient (HWHM, $\text{cm}^{-1} \text{atm}^{-1}$)
- h. Lower state energy (cm^{-1})
- i. Coefficient of temperature dependence, n , for air-broadened HWHM ($\gamma = \gamma_0 \times (296/T)^n$)
- j. Either the pressure shift ($\text{cm}^{-1} \text{atm}^{-1}$) or line-coupling coefficients
- k. Upper state global quanta index
- l. Lower state global quanta index
- m. Upper state local quanta
- n. Lower state local quanta
- o. Accuracy indices
- p. Indices for lookup of references

We use only fields a-j in our "100 character"-style files.

AVAILABILITY OF SAO92

The SAO92 database is available using ftp, upon request to K. Chance or K. W. Jucks. Magnetic tapes (9 track or Exabyte cartridges) can be furnished under special circumstances.

REFERENCES

1. L. S. Rothman, R. R. Gamache, A. Goldman, L. R. Brown, R. A. Toth, H. M. Pickett, R. L. Poynter, J.-M. Flaud, C. Camy-Peyret, A. Barbe, N. Husson, C. P. Rinsland, and M. A. H. Smith, *Appl. Opt.* **26**, 4058-4097 (1987).
2. L. S. Rothman, R. R. Gamache, R. H. Tipping, C. P. Rinsland, M. A. H. Smith, D. Chris Benner, V. Malathy Devi, J.-M. Flaud, C. Camy-Peyret, A. Perrin, A. Goldman, S. T. Massie, L. R. Brown, and R. A. Toth, *J. Quant. Spectrosc. Radiat. Transfer* **48**, 469-507 (1992).

3. Submillimeter, millimeter, and microwave spectral line catalog, R. L. Poynter and H. M. Pickett, *Publ. 80-23, revision 2*, Jet Propulsion Laboratory, Pasadena, CA, 1984; values current as of July 1992 obtained by FTP.
4. I. G. Nolt, J. V. Radostitz, G. DiLonardo, K. M. Evenson, D. A. Jennings, K. R. Leopold, M. D. Vanek, L. R. Zink, A. Hinz, and K. V. Chance, *J. Molec. Spectrosc.* **125**, 274-287 (1987).
5. D.A. Jennings, K.M. Evenson, M.D. Vanek, I.G. Nolt, J. V. Radostitz, and K.V. Chance, *Geophys. Res. Lett.* **14**, 722 (1987); erratum *Geophys. Res. Lett.* **14**, 981 (1987).
6. K. V. Chance, W. A. Traub, K. W. Jucks, and D. G. Johnson, *Int. J. IR and MM Waves* **12**, 581-588 (1991).
7. K. V. Chance, D. A. Jennings, K. M. Evenson, M. D. Vanek, I. G. Nolt, J. V. Radostitz, and K. Park, *J. Mol. Spectrosc.* **146**, 375-380 (1991).
8. K. Park, K. V. Chance, I. G. Nolt, J. V. Radostitz, M. D. Vanek, D. A. Jennings, and K. M. Evenson, *J. Molec. Spectrosc.* **147**, 521-525 (1991).
9. K. V. Chance, T. D. Varberg, K. Park, and L. R. Zink, *J. Molec. Spectrosc.* **162**, 120-126 (1993).
10. K. Chance, P. De Natale, M. Bellini, M. Inguscio, G. Di Lonardo and L. Fusina, *J. Molec. Spectrosc.*, in press (1993).
11. T. D. Varberg and K. M. Evenson, *Astrophys. J.* **385**, 763-765 (1992).
12. A. S. Pine and J. P. Looney, *J. Molec. Spectrosc.* **122**, 41-55 (1987).
13. G. Di Lonardo, L. Fusina, P. De Natale, M. Inguscio, and M. Prevedelli, *J. Molec. Spectrosc.* **148**, 86-92 (1991).
14. M. Carlotti, G. Di Lonardo, L. Fusina, A. Trombetti, and B. Carli, *J. Molec. Spectrosc.* **141**, 29-42 (1990). The HOCl on the database still includes some lines that we don't calculate, including lines with $J > 50$ and/or $K_a > 6$, a -type Q branch lines and $\Delta K_a = 3$ Q branch lines. The HITRAN92 position values are retained for these.
15. F. Masset, L. Lechuga-Fossat, J.-M. Flaud, C. Camy-Peyret, J. W. C. Johns, B. Carli, M. Carlotti, L. Fusina and A. Trombetti, *J. Phys. France* **49**, 1901-1910 (1988).
16. E. A. Cohen and H. M. Pickett, *J. Molec. Spectrosc.* **87**, 582-583 (1981).
17. P. B. Davies, B. J. Handy, E. K. Murray Lloyd, and D. R. Smith, *J. Chem. Phys.* **68**, 1135-1137 (1978).
18. R. J. Saykally and K. M. Evenson, *J. Chem. Phys.* **71**, 1564-1566 (1979); corrected position given in D. M. Watson, R. Genzel, C. H. Townes, M. W. Werner, and J. W. V. Storey, *Astrophys. J. Lett.* **279**, L1-L4 (1984).

FIGURE CAPTIONS

Figure 1. Summary of fitting of FIRS-2 balloon flight spectra from Fort Sumner, NM (fall 1989) used to obtain atmospheric concentration profiles. This figure provides a visual summary of most of the current thermal infrared stratospheric measurement capability.

Figure 2. A typical portion of a summed limb-scan of FIRS-2 spectra from the fall 1989 flight, illustrating the level of detail available in this type of measurement. This portion of the summed limb-scan (50 min. integration per spectrum; signal to noise ratio >500), from $99-100\text{ cm}^{-1}$, includes emission lines from the entire dynamic range of far infrared measurement capability, from the very strong H_2O lines near 99.1 cm^{-1} , to the very weak lines visible at below the 1% level of the spectra.

Figure 3. The result of an analysis of FIRS-2 data to determine the largest measurable far infrared features of those species we measure in our spectra (including one upper limit, HBr). This analysis represents the average midday observing conditions of Figs. 1 and 2. for an atmospheric tangent height of 32 km. This altitude is chosen because it is representative of mid-stratospheric conditions and it is the best altitude for FIRS-2 measurements to support this type of analysis. For convenience in discussing far infrared atmospheric measurements, the approximate limits where lines are fully saturated and fully unsaturated are noted on the figure. The current detection limit for the FIRS-2 instrument (appropriate for several hours of integration time, i.e., the most that can reasonably be obtained at one observation angle during a balloon flight) is also noted.

TABLE 1. Summary of SAO92 Molecular Line Database

| Mol. | Number | Source | Notes |
|------------------|--------|------------------|---|
| H ₂ O | 1 | HITRAN92 | 161 isotopic species only. H ₂ O @ 101.3197 — 101.3236. H ₂ O @ 178.9045 — 178.9071. H ₂ O @ 163.9602 — 163.9650. H ₂ O @ 204.5760 — 204.5750. |
| CO ₂ | 2 | HITRAN92 | Intensity (296 K) $\geq 10^{-25}$. |
| O ₃ | 3 | HITRAN92 | 666 isotopic species, vibrational ground state |
| N ₂ O | 4 | HITRAN92, SAO | Intensities for ν_2 fundamental transitions from J. W. C. Johns, private communication, 1993. Everything else from HITRAN92. |
| CO | 5 | SAO, HITRAN92 | Positions for ¹² C ¹⁶ O fundamental from TuFIR work; ¹¹ everything else from HITRAN92. |
| CH ₄ | 6 | HITRAN92 | Intensity (296 K) $\geq 10^{-27}$. |
| O ₂ | 7 | HITRAN92, JPLSMM | ¹⁶ O ¹⁶ O intensities and positions of (0-0) and (1-1) from JPLSMM where available; others from HITRAN92; all pressure-broadening from HITRAN92. ¹⁶ O ¹⁸ O 10-100 cm ⁻¹ from JPLSMM; above 100 cm ⁻¹ from HITRAN92; all pressure-broadening from HITRAN92. ¹⁶ O ¹⁷ O is all HITRAN92. |
| NO | 8 | HITRAN92 | HITRAN92 only goes to 100 cm ⁻¹ . |
| SO ₂ | 9 | HITRAN92 | Intensity (296 K) $\geq 10^{-21}$; this cutoff deletes all lines between 90.73 and 466.60 cm ⁻¹ . |
| NO ₂ | 10 | HITRAN92, JPLSMM | 10-200 cm ⁻¹ from JPLSMM; intensity (296 K) $\geq 10^{-23}$; pressure-broadening $\equiv 0.067$ (from HITRAN92). 580-800 cm ⁻¹ from HITRAN92; intensity (296 K) $\geq 10^{-23}$. |
| NH ₃ | 11 | HITRAN92 | Intensity (296 K) $\geq 10^{-20}$. |
| HNO ₃ | 12 | HITRAN92 | Intensity (296 K) $\geq 10^{-22}$. |
| OH | 13 | JPLSMM, SAO | ¹⁶ OH, ¹⁶ OD, ¹⁸ OH. Widths from TuFIR 118.455 measurement (including temperature dependence). ⁷ Positions from JPLSMM except for ¹⁶ OH 118.455 line. ⁷ |
| HF | 14 | HITRAN92, SAO | TuFIR positions up to R(4), ⁴ HITRAN92 above; intensities from SAO calculation; widths in SAO92 calculated to give correct Ref. 12 results at 230 K using $n = 0.67$ and interpolating with a power law. Widths and their temperature dependences for SAO92A are from Ref. 12 directly. All hot band parameters are from HITRAN92. |

| Mol. | Number | Source | Notes |
|-------------------------------|--------|---------------------|---|
| HCl | 15 | SAO, HITRAN92 | TuFIR positions, intensities from SAO calculation up to $R(11)$ (these include quadrupole splittings); ⁴ HITRAN92 (which does not include quadrupole) above. Widths from Ref. 12 up to $R(10)$; HITRAN92 above. Widths for SAO92 calculated to give correct Ref. 12 results at 230 K using $n = 0.67$. Ref. 12 widths and their temperature dependences used directly in SAO92A. Chlorine isotope ratio = .7576/.2423. All hot bands parameters from HITRAN92. |
| HBr | 16 | SAO, HITRAN92 | Positions for fundamental below 200 cm^{-1} from TuFIR measurements; ¹³ higher fundamental and all hot band positions from HITRAN92. Intensities for rotational fundamental from SAO dipole moment calculation; hot band intensities from HITRAN92. All widths from HITRAN92. |
| HI | 17 | HITRAN92 | |
| ClO | 18 | HITRAN92 | |
| OCS | 19 | HITRAN92 | |
| H ₂ CO | 20 | HITRAN92 | Intensity (296 K) $\geq 10^{-22}$. |
| HOCl | 21 | SAO, HITRAN92 | Positions for most (i.e., the strongest) lines calculated from constants in Ref. 14; the rest are from HITRAN92. All intensities and widths from HITRAN92. No SAO92 lines; included for completeness. |
| N ₂ | 22 | HITRAN92 | |
| HCN | 23 | HITRAN92 | |
| CH ₃ Cl | 24 | HITRAN92 | No SAO92 lines; included for completeness. |
| H ₂ O ₂ | 25 | SAO | RQ_4 (94 cm^{-1}) and RQ_5 (112 cm^{-1}) only. Positions calculated from Ref. 15 (J.-M. Flaud, private communication); intensities from dipole moment; ¹⁶ widths arbitrarily set to 0.1. Note that far infrared positions in HITRAN92 are demonstrably incorrect and that the Q branches are not included. |
| C ₂ H ₂ | 26 | HITRAN92 | No SAO92 lines; included for completeness. |
| C ₂ H ₆ | 27 | HITRAN92 | No SAO92 lines; included for completeness. |
| PH ₃ | 28 | HITRAN92 | No SAO92 lines; included for completeness. |
| O ₃ ISO | 29 | HITRAN92, JPLSMM | 668 and 686 are HITRAN92. 667 and 676 are JPLSMM ($676\text{ only goes to }139\text{ cm}^{-1}$); widths for 667 and 676 set to 0.07; isotopic abundance for 667 is 0.00074; isotopic abundance for 676 is 0.00037 |
| HOTO ₃ | 30 | HITRAN92 | HOTO ₃ @ $112.1909 \rightarrow 112.1900$ HOTO ₃ @ $112.3404 \rightarrow 112.3402$ HOTO ₃ @ $112.3611 \rightarrow 112.3606$ HOTO ₃ @ $112.3930 \rightarrow 112.3924$ |
| O ³ P | 31 | SAO | Corrected positions ^{17,18} |

| Mol. | Number | Source | Notes |
|-------------------------------|--------|-----------------------|---|
| HO ₂ | 32 | SAO, JPL | TuFIR-measured line positions (which include all FIRS-2 measured atmospheric lines) included. Other positions, all intensities, calculated from JPL Hamiltonian (H. M. Pickett, private communication). Intensity (296 K) $\geq 10^{-24}$. |
| H ₂ OIS | 33 | HITRAN92 | Minor isotopomers other than HDO. |
| O ₂ ¹ D | 34 | JPLSMM | O ₂ (¹ Δ) |
| DUMMY | 35 | | Used to make dummy lines (see text). |
| HDO | 36 | HITRAN92. HITRAN82 | Separated out from H ₂ OIS for convenience in spectrum fitting. Lines above the one at 100.4901 are from HITRAN82 (they were left out of HITRAN92). HDO @ 112.299 — 112.298 |

